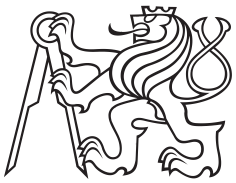

Czech
Technical
University
in Prague

F4

Faculty of Nuclear Sciences and Physical Engineering
Department of Materials

Resonace and quasi-static bending tests of thermally sprayed and additively manufactured materials

Ondřej Kovářík

November 2025

Dennis Scott: What are you doing to it?
Theodore Honey: I'm vibrating it.

Koster H. (Director), (1951)
No Highway in the Sky [Film]
20th Century Fox

Acknowledgements

I would also like to express deep gratitude to colleagues that took me to the fascinating word of fatigue damage of materials and also to ones that guided me in its different application areas. Namely to Jan Siegl of Faculty of Nuclear Sciences and Physical Engineering, CTU and Pavel Chráska of IPP, CAS, who initiated the pioneering fatigue studies on specimens with thermally sprayed coatings. Maher Boulos of Université de Sherbrooke is gratefully acknowledged for bringing me to the thermal spray universe. Many of the studies described in this work could not have been performed without the enthusiasm of Jan Čížek of IPP, who actively promoted the bending test methods in the thermal/cold spray community. Ivan Tomáš of FZU, CAS brought the growing cracks into focus. Rhys Jones of Monash University quantitatively described the obtained data and put them in industry relevant context. Many thanks go also to colleagues from Stony Brook University, Impact Innovation GmbH, Poliecnico di Milano, Trinity College Dublin, University West, Unversité de Sherbrooke, Politechnika Wrocławska, Ponticon GmbH, Norteastern University in Boston and Helmut Schmidt Universität who provided their precious coatings and deposits for testing.

Last but not least I acknowledge the encouragement of my parents, Alena and Petr, who supported the early steps of my engineering journey. Equally cherished is the extraordinary patience and support of my wife Eliška and our children Terezka, František, and Antonín, whose presence lent both balance and inspiration.

in Mnichovice, November 17th, 2025

Abstract

Development of new classes of materials calls for the development of new testing methods. Two resonance based fatigue test methods developed at department of materials, Faculty of Nuclear Sciences and Physical Engineering, Czech Technical University in Prague, in the last years are presented: bending of surface treated flat cantilevers to obtain fatigue life/strength and pure bending of small rectangular specimens to study the fatigue crack propagation rate. Additional quasi-static bending methods of small specimens for the measurement of stress-strain properties and fracture toughness are also described. The basic principles, specific qualities, advantages and limitations of the methods are summarized. The methods are illustrated on published studies concerning fatigue life of surface treated materials as well as mechanical and fracture properties of additively manufactured materials.

Keywords: fatigue strength, fatigue crack growth, fracture toughness, stress-strain curve, differential compliance, resonance, small specimens

Contents

List of Symbols 1
List of Abbreviations 2

1 Introduction **3**

2 Flat, surface treated specimens **7**
2.1 Fatigue life test 7
2.2 Results 9
2.2.1 Single deflection amplitude testing 9
2.2.2 Multiple deflection amplitude testing 12

3 Small specimens **15**
3.1 Fatigue crack growth rate test method 15
3.1.1 Excitation 16
3.1.2 Crack length measurement 18
3.1.3 Test modes 25
3.1.4 Fatigue test protocol 26
3.1.5 Validation of the testing method 27
3.1.6 Peculiarities of the method 29
3.1.7 Fatigue crack growth rate data model 33
3.2 Fracture toughness 34
3.3 Stress-strain 35
3.4 Results 37
3.4.1 Plasma spray 37
3.4.2 Cold spray 39
3.4.3 Modelling of fatigue crack growth rate 42
3.4.4 Directed energy deposition 43

4 Conclusions and Outlook **45**

5 References **47**
5.1 Flat specimen references 47
5.2 Small specimen references 49
5.3 Other references 52

List of Symbols

α	yoke rotation angle	rad
$\ddot{\alpha}$	yoke angular acceleration	$\mathrm{rad\,s^{-2}}$
α_{crack}	additional yoke rotation caused by crack	rad
α_{max}	maximum α for open crack	rad
α_{min}	minimum α for closed crack	rad
α_{oc}	α for transition of closed into open crack	rad
$\frac{\mathrm{d}a}{\mathrm{d}N}$	fatigue crack growth rate	$\mathrm{m\,cycle^{-1}}$
A	dynamic fracture tougness	$\mathrm{MPa}\sqrt{\mathrm{m}}$
A_{o}	vibration amplitude of α for open crack	rad
A_{c}	vibration amplitude of α for closed crack	rad
a	crack length	m
a_n	notch depth	m
b	specimen thickness	m
b	specimen width	m
C	angular acceleration offset	$\mathrm{rad\,s^{-2}}$
c	specimen compliance	rad/Nm
c_{n}	notch compliance	rad/Nm
c_{o}	c of specimen with open crack	rad/Nm
c_{c}	c of specimen with closed crack	rad/Nm
c_{crack}	crack added compliance	rad/Nm
E	elastic modulus	GPa
f	geometric function of finite body	1
I	second moment of area of speciemn cross section	$\mathrm{m^3}$
J_y	yoke moment of inertia to its axis of rotation	$\mathrm{kg\,m^2}$
G	elastic energy released by crack advance	J/m
σ	nominal bending stress	MPa
σ_{max}	maximum value of σ of loading cycle	MPa
σ_{oc}	σ at crack opening	MPa
K	stress intensity factor	$\mathrm{MPa}\sqrt{\mathrm{m}}$
K_{I}	mode I stress intensity factor	$\mathrm{MPa}\sqrt{\mathrm{m}}$
ΔK	stress intensity factor range	$\mathrm{MPa}\sqrt{\mathrm{m}}$
ΔK_{thr}	threshold value of stress intensity factor range	$\mathrm{MPa}\sqrt{\mathrm{m}}$
ΔK_{th}	threshold value of stress intensity factor range at $\frac{\mathrm{d}a}{\mathrm{d}N} = 1 \times 10^{-10}\,\mathrm{m\,cycle^{-1}}$	$\mathrm{MPa}\sqrt{\mathrm{m}}$
K_{max}	maximum value of stress intensity factor of loading cycle	$\mathrm{MPa}\sqrt{\mathrm{m}}$
K_{oc}	stress intensity factor at crack opening load	$\mathrm{MPa}\sqrt{\mathrm{m}}$
ΔK_{eff}	effective value stress intensity factor	$\mathrm{MPa}\sqrt{\mathrm{m}}$

ΔK_{ACR}	effective value stress intensity factor evaluated by adjusted compliance ratio [41]	$\mathrm{MPa}\sqrt{\mathrm{m}}$
ΔK_{IC}	fracture toughness	$\mathrm{MPa}\sqrt{\mathrm{m}}$
M_r	reaction moment caused by specimen bending	$\mathrm{N\,m}$
M_t	loading moment caused by yoke acceleration	$\mathrm{N\,m}$
M_{oc}	loading moment causing crack opening	$\mathrm{N\,m}$
ν	Poisson's ratio	1
ω	angular frequency of vibration	$\mathrm{rad\,s^{-1}}$
ω_o	ω for open crack part of cycle	$\mathrm{rad\,s^{-1}}$
ω_c	ω for closed crack part of cycle	$\mathrm{rad\,s^{-1}}$
Φ	nondimensional compliance	1
φ	phase shift	rad
R_n	notch radius	m
$R_{p0.2}$	0.2%offset yield strength	MPa
R	remote load ratio $R = \frac{\sigma_{\min}}{\sigma_{\max}}$	1
τ	phase coordinate of the loading cycle	rad
τ_{oc}	τ at crack opening	rad
$\mathrm{YS_t}$	yield strength in tension	MPa

List of Abbreviations

CAS	Czech Academy of Science
CS	cold spray
CSAM	cold spray additive manufacturing
CTU	Czech Technical University in Prague
DED	directed energy deposition
DIC	digital image correlation
EBSD	electron backscatter diffraction
EDM	electric discharge machining
FNSPE	Faculty of Nuclear Sciences and Physical Engineering
FCGR	fatigue crack growth rate
FZU	Institute of Physics, CAS
IPF	inverse pole figure by EBSD
IPP	Institute of Plasma Physics, CAS
LFM	linear elastic fracture mechanics
MAT	magnetic adaptive testing
YSZ	yttria stabilized zirconia

Chapter 1

Introduction

Long before material science had developed, the knowledge of materials and their processing defined the way of life for humankind. Stone, bronze, and iron gave names to historical epoques spanning thousands of years. During the ages, the human ability to use materials has increased exponentially, and currently, new materials are being developed on a daily basis. As new materials emerged, so did their characterization techniques, and their portfolio increased from the medieval times of Georgius Agricola [42] to the present [43, 44].

The process continues, and today engineers have a great choice of materials as well as characterization techniques available. At the same time, new technologies in aerospace, power generation, bio-engineering, and electronics repeatedly call for the development of new materials with specific properties, such as high temperature, wear and corrosion resistance, bio-compatibility, heat conductivity, etc., to name just a few. To deliver such materials, new production routes are being developed that complement classical technologies. New bulk materials can be prepared effectively in small amounts by arc melting, sintering, near net thermal and cold spray deposition, and by other additive manufacturing techniques, such as selective laser melting and directed energy deposition, etc. The surface of the material can be modified by coating, grit blasting, shot-peening, or other surface conditioning techniques. On one hand, the above techniques offer much greater flexibility in the final shape of the product by eliminating some steps in the laborious and, hence, costly classical manufacturing routes such as casting, forging, machining, etc... On the other hand, the classical approach can take advantage of significant knowledge about the effects of process parameters gathered and formalized over the years. With emerging technologies, such knowledge is rarely available. Therefore, selecting a particular process and its parameters is often extremely difficult. The selection process can be based on so called process maps that relate material properties to process parameters [45]. Many process maps are being developed for new combinations of technologies and materials, and general principles are being investigated that allow for the explanation of the underlying phenomena [46]. So far, the concept of process maps has been successfully used in thermal spray, but it is gaining importance in other areas, regardless of whether bulk or surface modified material is investigated.

The exploration of the process space, e.g., a factorial experiment with many degrees of freedom, naturally calls for flexible testing techniques with low demands on the quantity of tested material and simple sample geometry. It is imperative that the testing method is based on a small volume of the tested materials, as there is usually a small quantity of them available at any given point in the process space. At the same time, multiple tests are often desired at different locations and orientations to assess the isotropy and homogeneity of the tested material.

Not only new materials require small specimens. Many 'old' materials that survived as fragments of tools, art-pieces, weapons, and machines are also worth testing. Also 'worn' materials, such as those from nuclear surveillance programs [47] or accident investigations [48], have very limited availability.

The classical stress-strain properties can be evaluated from small specimens, typically by instrumented indentation [49], small punch tests [50], ball indentation tests [51], as well as tensile tests [52, 53] or bending tests [54]. A recent review [55] classifies the stress-strain tests of small specimens into **similarity** (scaled tensile and bending tests), **penetration** (small punch tests, including notched geometries without rotational symmetry), and **semi-penetration** test classes (indentation methods). From these classes, similarity methods provide the simplest description of loading stress and enable direct measurement of all characteristics of basic materials, namely elastic modulus E, yield strength $R_{p0.2}$, and ultimate tensile strength R_m.

The measurement of fracture properties is based on linear elastic fracture mechanics (LFM), especially if cyclic loading is considered. The fundamental overview of the problem is summarized in [56]. It stresses the importance of the relationship between the size of the stress intensity factor dominated zone and the microstructural characteristics of the materials (such as splats, grains, melt pools, etc.) as well as the dimensions of the specimen. Similarity based fracture tests of nuclear materials are summarized together with stress-strain tests in [57] including mini tensile, bending, and CT specimens.

Many small specimen tests have already been included in international standards. One prominent example is the new supplement to the ASTM E8 standard [58], which provides guidelines for testing miniature tensile specimens. This method is well suited for AM materials as shown in a round robin study for 316 and 4340 steels [59], where the test results were well comparable between multiple specimen sizes.

Specifically, for thermal spray and additive manufacturing, the appropriate testing methods are summarized in reviews that cover thermal spray [60], cold spray [61], and additive manufacturing [62]. From all the methods described in the above reviews, the stress-strain behavior, fracture toughness, fatigue properties, and hardness are appreciated to provide valuable information for both design and research. Specific testing methods are also necessary for the area of surface engineered material where the surface and the underlying substrate form a system that should be investigated together.

This work is focused on the development of bending methods of small specimen testing, however, its also includes bending methods for standard size

surface modified specimens (generally with thermally sprayed coatings) that were developed first and shaped the small specimen bending methods later. The applications of these methods to test coated and surface treated materials as well as additively manufactured (plasma and cold sprayed, directed energy deposited, powder bed fused) materials are also summarized.

The testing methodology for surface treated materials used relatively large flat specimens (see Fig. 2.1) that can be easily tested in the as-sprayed or grit-blasted state without any sectioning or other modification. These specimens will be referred to as **flat** throughout this work. The flat specimen part of this work will focus on the development of an efficient testing method that allowed us to obtain interesting information on the fatigue properties of coated or surface treated materials published in several works [1–11].

The following bending test methods for flat specimens of surface modified materials were implemented:

stress-strain - the coating properties can be extracted from the four point bending of the substrate - coating composite using the method of Rybicky et al [63],

thermal expansion - the coating-substrate composite beam was heated to an uniform elevated temperature and the radius of curvature caused by the thermal mismatch was measured and transformed into the elastic modulus of the coating or its thermal expansion coefficient [12],

fatigue test - flat dogbone shaped specimens were loaded as cantilever beams to establish fatigue strength at a given load or the complete S-N curve.

The development of additive manufacturing techniques such as cold spray calls for testing materials of near net shape deposits or additive manufactured parts, bringing the bulk material itself under focus. The small specimen bending methodology was developed especially for these materials in order to enable testing of small material quantities produced on a laboratory scale. The methodology consists of three independently performed types of test that are all based on the bending of the same small rectangular beams. Therefore, it is referred to as **small** specimen methodology below. The bending mode of loading was chosen because it does not require provisions for clamping such as threads, locks, etc., and therefore very simple rectangular specimen geometry can be used. In turn, such geometry allows for easy surface finish should it be required by the test methods. The methodology consists of:

stress-strain - four point bending instrumented with digital image correlation providing “uniaxial” stress using an approach of Herbert [64],

fatigue crack growth rate test - resonance test of a notched specimen loaded in pure bending to nucleate a fatigue crack and study its growth rate as a function of the crack propagation driving force [18],

fracture toughness - fracture toughness test performed following ASTM E1820 standard [65] on fatigue precracked samples.

The above methods were used to test different types of materials, and the results are summarized in [18–39].

Chapter 2

Flat, surface treated specimens

2.1 Fatigue life test

The influence of surface treatment on the fatigue lifetime of coated bodies has been studied by different methods [66–76] over the years. In the above mentioned works, the bending loading is generally used as it invokes maximum stress at the coated specimen surface, which makes the testing methods sensitive to surface treatment or coating properties. These bending setups are often based on rotational bending of round specimens or cantilever bending of flat specimens. The fatigue performance of surface treated materials is characterized by fatigue strength at single load or by fatigue strength diagrams (S-N curves). In order to speed up the testing, high test frequencies are desired, which can be achieved with rotational bending or resonance testing.

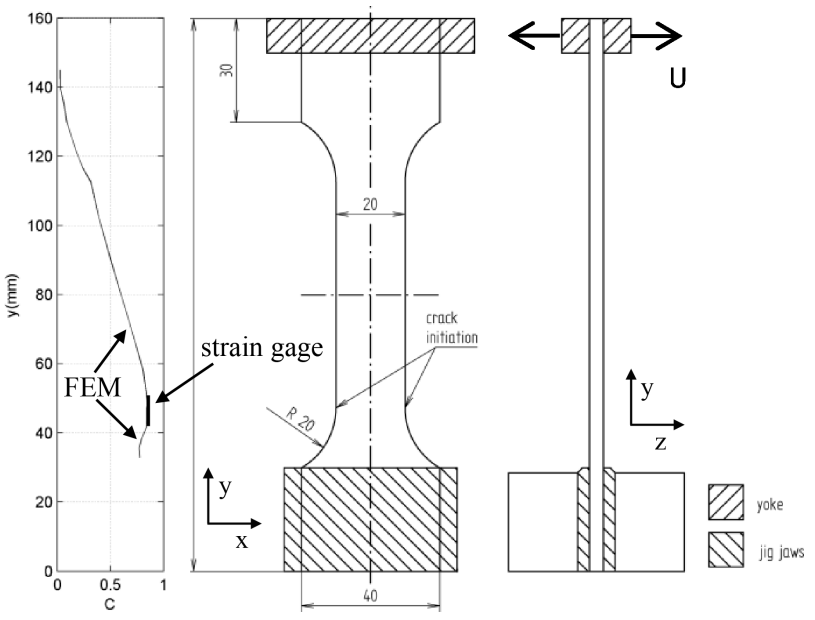

Figure 2.1: Schematic drawing of the dogbone flat specimen used for fatigue testing in [9].

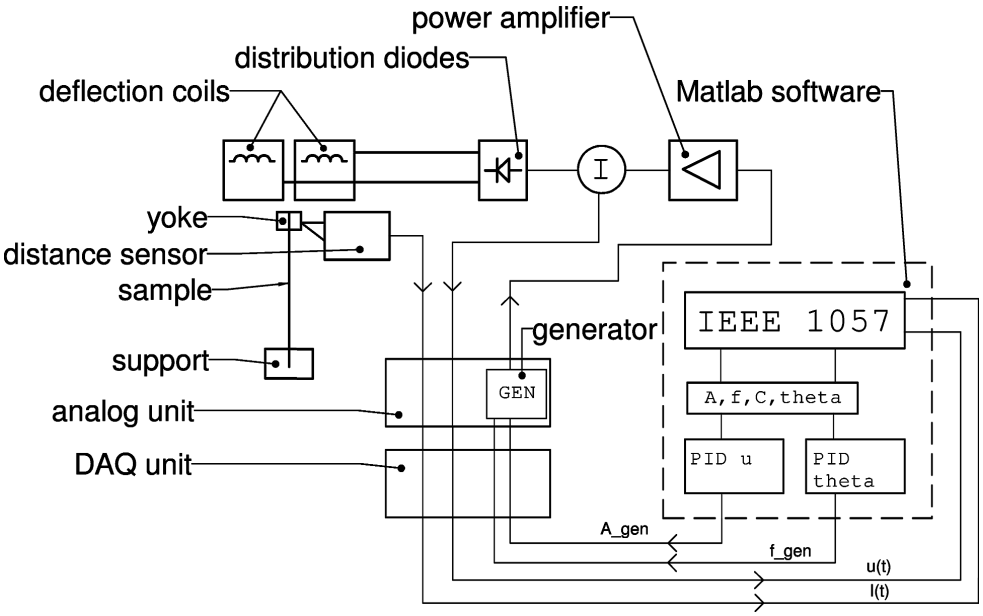

Figure 2.2: Schematic drawing of the control system of the SF-test surface fatigue testing device from [8].

In resonance testing, the repeated transformation of elastic and kinetic energy called resonant vibration is utilized. This approach allows for gradual excitation of the dynamical system with relatively low power compared to hydraulic or servomechanical loading, where the system must be able to provide the power necessary for instantaneous specimen loading to the target load at high loading rates. For small specimens that inherently require lower loads, electrodynamical systems pioneered by Bose [77] can provide sufficient power and higher flexibility than resonance systems. Nevertheless, the resonance approach can bring significant simplification and miniaturization of the loading setup desired for testing in vacuum or in various other environments, eventually for in-situ measurements such as neutron or X-ray diffraction. Moreover, the resonance frequencies of the testing system are related to the changes of the sample such as the dynamic modulus defect and crack growth [13]. Therefeore, the resonant vibration test is a very attractive measurement method combining both the sample excitation and the measurement of its properties at the same time.

In the department of materials, FNSPE, CTU, the resonance cantilever setup using symmetrical dog-bone shaped specimens was gradually developed to the form shown in Fig. 2.1. The system consists of a vibrating cantilever beam with tip mass excited by an alternating electromagnetic field invoked by two air coils. The strain at the lower end of the gage section is proportionally related to the free end deflection as $\varepsilon = 100 \times C \times u \times h$ where u is the free end deflection, h is the specimen thickness and $C = 0.844$ is the multiplication coefficient estimated by FEA modal analysis [10]. The vibration of the cantilever was maintained by the phase locked loop technique implemented using an analog cirtcuit that was later replaced with fully digital phase

discriminator based on the IEEE1057 standard [78], see Fig. 2.2.

The system was subsequently equipped with a synchronized camera setup that enables the specimen surface to be captured in an arbitrary phase of the loading cycle for digital image correlation analysis (DIC) [9].

2.2 Results

2.2.1 Single deflection amplitude testing

To assess the influence of coating of fatigue life, the tests of constant fixed free end deflection amplitude were performed. This type of loading ensures that the substrate in the stress concentration area is loaded by an equal strain range regardless of the applied coatings. In most tests, the standard deflection of 4 mm corresponding to a surface strain of about 1.3×10^{-3} and stress is steel substrates equal to 280 MPa was used.

Plasma sprayed ceramics on steel

The effect of thermally sprayed coatings on fatigue lifetime was studied for alumina coatings deposited on low carbon steel substrates using the water stabilized plasma torch (WSP) [1]. The coating deposition process inherently includes grit-blasting as a means of cleaning and roughening of the substrate to achieve sufficient adhesion. Therefore, the fatigue life of the coated bodies was compared with that of the as-rolled and grit-blasted substrates. Plasma coated specimens showed longer fatigue lives than grit-blasted and as-rolled substrates. The effect of grit-blasting was found to be negligible. Splat breaking and decohesion as well as void coalescence were identified as the coating failure mechanism. No clear fractographic signs indicating fatigue in the coating were found, and thus the sequence of substrate/coating failure could not be identified. The weak effect of grit blasting was somehow surprising, but it was concluded that deformation induced strain hardening, residual stress, and micronotch formation in the surface area of the substrate can act against each other and thus minimize the resulting change in fatigue performance. Later, a separate study was performed to quantify these effects [14]. In this study, all three above effects of grit-blasting were detected and quantified.

Thermally sprayed metals and ceramics on steel

A similar methodology was applied for testing various thermal spray coatings deposited by a variety of techniques in [2]. Plasma sprayed ceramics, namely alumina, chromia, and olivine, were tested. Metallic materials included plasma sprayed molybdenum as well as Ni5wt%Al coatings deposited by wire arc, plasma, and high velocity oxygen fuel (HVOF). Ceramic coatings were found to increase fatigue life, while the effect of the metallic coating was neutral or negative. The single exception was the Ni5wt%Al deposited by

HVOF that significantly increased fatigue life. The results indicated that the increases in fatigue life for metallic coatings can be related to the coating residual stress. This relation was not observed for ceramic coatings, where significantly lower residual stresses were observed. The failure mechanism of the coating was similar to that described for alumina, and again no clear fractographic signs could be identified in the coatings. The stiffness of the specimen was found to change not only due to the crack growth, but also due to the transient effect. After the interruption of the experiment, the transient stiffness decrease was restored. Energy dissipation was also found to gradually increase during the crack initiation stage of the test to a saturated level, while it becomes nearly constant in the fatigue crack propagation stage (see Fig. 2.3). Further studies of this phenomenon were performed using magnetic adaptive testing (MAT) methods [15, 16]. The MAT method characterizes fatigue damage through a microdegradation function. The microdegradation function is the derivative of permeability obtained from a minor hysteresis loop at given magnetizing current. Many microdegradation functions are available and the ones most sensitive to observed damage are then evaluated. In the first study [15] repetitive in-situ measurements were performed during interrupted fatigue experiments, the second study was based on a series of samples, fatigued to a certain proportion of the expected fatigue lifetime, enabling the use of a more flexible ex-situ measurement method. The results of both studies indicated a similar trend of the magnetic parameters, i.e. their changes in the crack initiation phase leading to saturation (see the initial property changes in Figures 2.3 and 2.4).

The identical single deflection methodology was used for the study of FeAl intermetallic coatings of different compositions deposited by WSP and conventional gas atmospheric plasma spray (APS) system in [17]. These metallic coatings showed fatigue lives shorter than the reference series, i.e., a similar behavior to the metallic deposits tested before in [1, 2].

Two major fracture mechanisms of individual coatings were identified. Both of these mechanisms were active in all observed coatings, and their occurrence was dependent on the particular combination of feedstock material and deposition technology. Trans-splat fracture, often following the columnar grain structure, was common in ceramic deposits and Mo metallic coatings, as well as in Fe Al intermetallics. A significant amount of inter-splat decohesion was observed in N5wt%Al deposits.

Cr_2O_3 and Ni-5Al multilayers on steel

The above studies indicated that the influence of ceramic and metallic coatings is qualitatively different and that in most of the investigated cases the ceramic coating increased, whereas the metallic coatings decreased fatigue lifetimes. Therefore, different failure mechanisms were considered for these two types of coating. A detailed study focused on failure of plasma sprayed layered deposits of chromia and Ni5wt%Al [5]. The effect of the first and second deposited layers on fatigue life was determined using statistical methods. However, the mechanism of this influence was not uncovered despite the

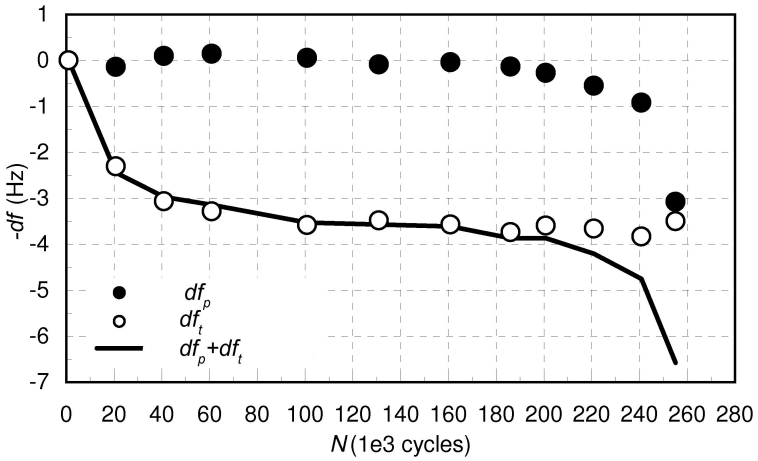

Figure 2.3: Frequency changes observed during interrupted testing of low carbon steel in [2]. Full dots represent transient change df_t, empty dots indicate permanent change df_p, solid line is the sum of both.

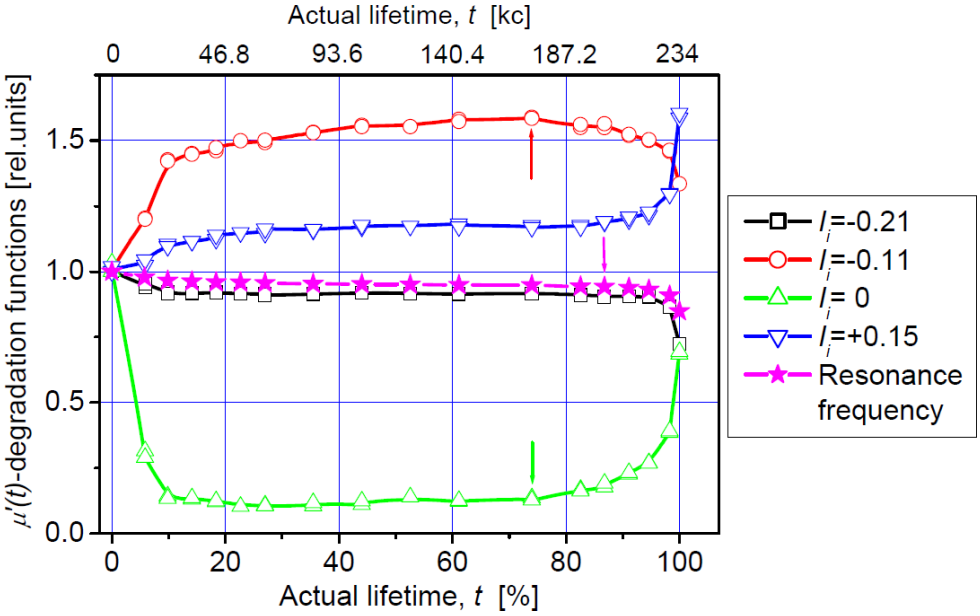

Figure 2.4: Microdegradation function $\mu\prime(t)$ measured on low carbon steel specimen during ther interrupted fatigue experiment in [15]

detailed measurement of hardness and residual stresses in the substrate. The hypothesis of localized damage in the metallic layers and distributed damage in the ceramic layers was formed.

Low carbon steel substrates were also utilized in a study [7] focused on pure Ti coatings deposited by plasma, cold spray, and warm spray technologies. Somehow incoherently with the results above, the metallic coating significantly improved the fatigue life for all three deposition technologies. Again, the fractography of the coating did not reveal any clear signs of fatigue in the coating.

Plasma sprayed Ti on Ti-6Al-4V

To assess the fatigue performance of Ti-6Al-4V coated by pure Ti for biomedical and aerospace applications, a series of tests were performed using plasma spray and cold spray [4]. The loading amplitude $u = 7\,\text{mm}$ corresponded to $\varepsilon = 2.35 \times 10^{-3}$ and thus $\sigma = 260\,\text{MPa}$. Here, in contrast to steel substrates, the loading is much lower than the yield strength $R_{p0.2} \approx 900\,\text{MPa}$. Interestingly, both types of coating decreased fatigue lifetime, in contrast to similar coatings deposited on low-carbon substrates later in [7] that showed an increase in fatigue lifetime. For the first time, coating fractography was able to identify areas where crack surfaces were in periodic contact. Thus, it was confirmed that coating failure can take place during the fatigue lifetime and is not formed exclusively by the final static fracture.

The tests performed on steel and Ti-6Al-4V substrates later (see [7]) clearly indicated the influence of the coating on fatigue life at the tested deformation amplitude. However, it was impossible to attribute the fatigue life change to a specific effect of the coatings or the coating process. It was concluded that fatigue performance is given by the deformation and failure mode of the coating, as well as by the changes experienced by the substrate surface layer during grit-blasting and deposition including the formation of residual stress. However, the results obtained did not allow for the clear identification and quantification of the underlying mechanisms.

2.2.2 Multiple deflection amplitude testing

TBC on steel

The first pilot study to establish an analogy to S-N fatigue curve was focused on yttria stabilized zirconia thermal barrier coatings (TBC), namely on the influence of each deposition stage, i.e. blasting, bond-coat and top-coat on fatigue lifetime. Steel substrates used in this pilot study to check the feasibility of the approach before expensive Hastelloy-X substrates relevant for industrial application were prepared [6]. In this paper, the fatigue lifetime was related to the free end deflection to show that, contrary to the single amplitude at $u = 4\,\text{mm}$, grit blasting significantly increases the fatigue life at lower loading amplitudes. Adding NiCoCrAlY bond coat slightly increased the fatigue lifetime, and adding YSZ topcoat led to a further fatigue life increase.

TBC on Hastelloy-X

A similar experiment was performed on TBC's on industry relevant Hastelloy-X substrates (see [10]). This time, the strain range was related to lifetime; see Fig. 2.5. The results showed a significant improvement in fatigue lives after blasting, but the application of NiCrAlY bond coat brought it back to the reference level. Adding YSZ layer had no further effect. Heat treatment

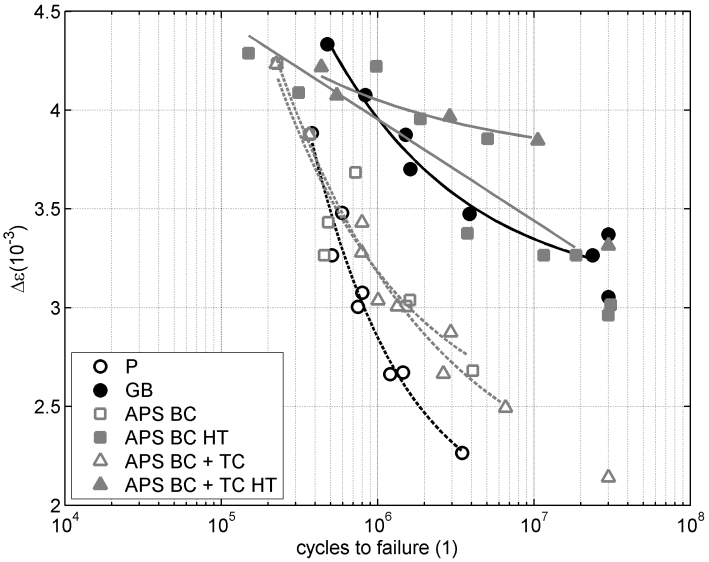

Figure 2.5: $\Delta\varepsilon - N$ curve of TBC coating on Hastelloy-X taken from [10], GB - grit blasting, BC - bond-coat, TC - top-coat, HT - heat treatment

applied to simulate in service conditions brought all coatings to a level comparable to that of grit blasted material, meaning a significant increase in fatigue lifetime over the as-received substrates.

Further studies were performed on the coated Hastelloy-X substrates. In the study [9] the kinetics of crack growth was systematically studied using DIC method. The crack initiation was clearly indicated and the propagation of fatigue crack of the different surface treatment was compared. It was concluded that the deposit influences the number of cycles N_i to crack initiation, but has a small effect on crack growth. The results of fractographic analysis, i.e. the preferable initiation on edges for grit-blasted specimens and the initiation on specimen faces for other coated specimens, were also confirmed. The shift from edge initiation for grit-blasted specimens to face initiation for coated specimens was attributed to nonhomogeneity of the deformation field caused by the presence of the nonhomogeneous coating. The effect of grit-blasting on crack propagation at low crack length was shown by fractographic analysis.

To further explore the failure process during fatigue loading, a specimen damping study was carried out in the course of the fatigue test [8]. The damping of the sample was found to increase much sooner than a measurable crack was detected. The fatigue life was divided into two phases for all samples. In the crack initiation phase, the damping increased, leading to temporary damping saturation. In the crack propagation phase, both the stiffness of the sample and the damping decreased. This confirmed the results of our early study [2], where the damping was indirectly observed using pyrometric measurement. Unfortunately, it appeared that the substrate damping is difficult to observe for coated specimens, as the coating also dissipates a

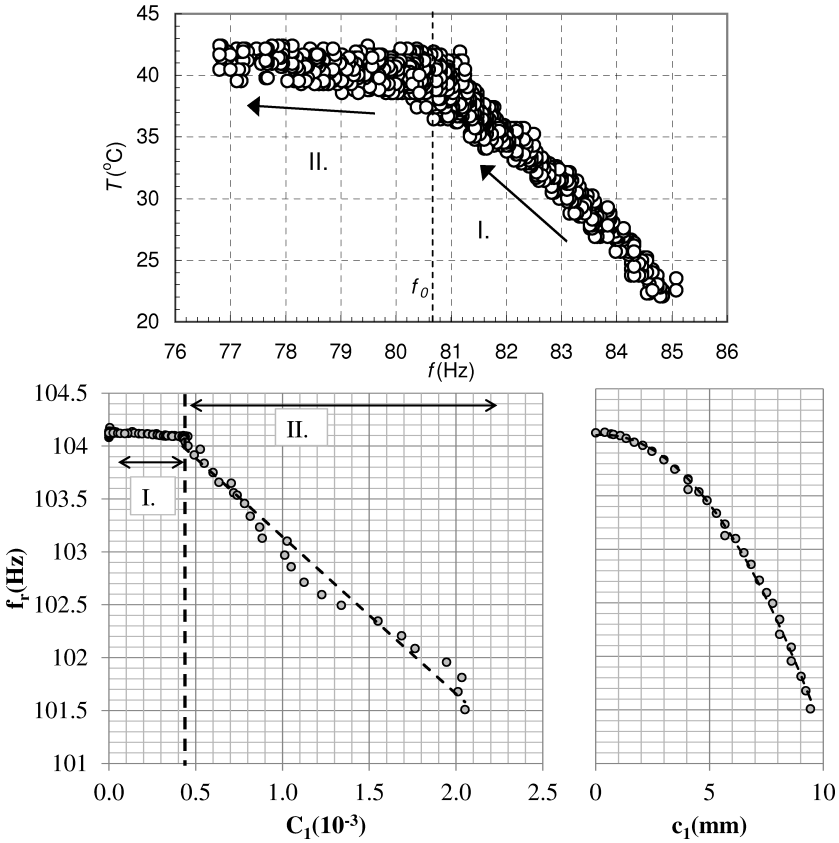

Figure 2.6: Fatigue crack initiation (I.) and propagation (II.) phases of fatigue life. $T(f)$ curve for grit-blasted steel specimen from [2] and $C_1(f)$ curve for grit-blasted Hastelloy-X specimen from [8]. Here T is specimen surface temperature, C_i is damping characteristics, c is specimen crack mouth length.

significant amount of energy. Based on this research, damping of the coating should be considered a parameter of the coating that may influence the fatigue properties.

The results of multiple amplitude tests clearly indicated that the effect of surface treatment must be regarded as load dependent, and further testing should be performed at multiple loads. In the experiments performed, the effect of the coating appeared to predominantly influence the crack initiation phase. The influence of grit-blasting on fatigue life was attributed to residual stress, work hardening, and surface roughness, whereas most of these effects are retained after coating deposition. The coating influence was attributed to its nonhomogeneity, leading to stress localization, as well as to its damping capacity.

Chapter 3

Small specimens

In this chapter, the methodology focused on the extraction of mechanical and fracture properties from a small quantity of material is described. The dimensions of the test specimen were selected so that the probed volume is significantly higher than the microstructural units of the tested materials, namely, splats, particles, and crystal grains. The universal specimen shape for all characterization methods presented in this chapter is a rectangular bar of dimensions 4 mm × 3 mm × 32 mm ($h \times b \times l$, see Fig. 3.1). This specimen geometry can be easily prepared by electric discharge machining (EDM). Its size enables one to address material anisotropy and nonhomogeneity, provided that the billet has at least 32 mm in each dimension. For in plane properties, the billet thickness of $h \geq 4$ mm is required. Methods for measuring fatigue properties, namely fatigue testing to obtain fatigue strength (not discussed in this thesis) and fatigue crack growth rate (FCGR) tests, were developed first [18, 19], followed by the other quasi-static testing methods, i.e., fracture toughness test and stress-strain bending test [21, 24]. The combination of measurement methods presented reflects the current state of the testing methodology that has been developed over the years and is described in the papers [18, 19, 39] for fatigue crack growth rate testing and in [20] for fracture toughness and stress-strain testing. The generated fracture data were later described by the Hartmann-Schijve formula in [33]. The format of this thesis allows for an even more detailed description of the methods, as well as a short discussion of the peculiarities of the small specimen methodology. Shortly before the completion of this thesis, it was realized that this extended description provides a solid base for a self contained journal paper; therefore, it was published as [39].

3.1 Fatigue crack growth rate test method

Following the success of the applied bending resonance testing of large flat coated specimens (see [1–11]), it was decided to develop the resonance method for the testing of small specimens. The small specimen research was first related to a project on nuclear pressure vessel steels [79] that required small 4 mm × 3 mm × 32 mm samples to be precracked before fracture toughness testing, as required by the ASTM E1820 standard [65]. The necessity to

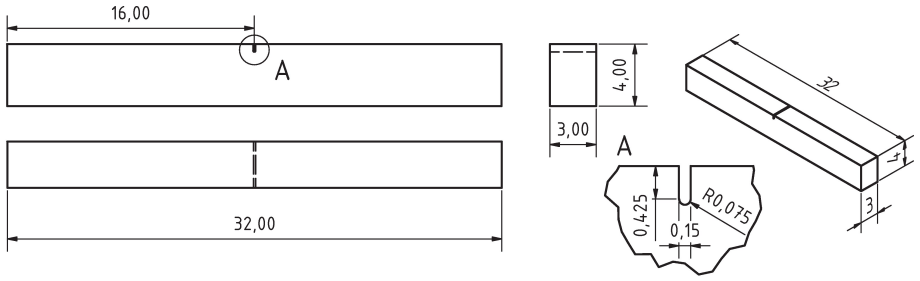

Figure 3.1: Dimension of the universal specimen, dimensions in mm, the notch is made on fracture toughness and fatigue crack growth rate specimens, the stress-strain specimens are without the notch.

stop crack growth at a given length required a robust method of crack length measurement. The simple relation of crack length to resonance frequency, as described in [2], could not be used, as the clamping compliance of the specimen and the dynamic modulus both decrease during the test (see [8] [80]), which in turn influences the resonance frequency. Therefore, the differential compliance method [81] , which eliminates these factors, was used to measure the crack length. The method is based on the compliance difference of specimen states with open and closed cracks. No calibration is necessary, as the reference compliance (fatigue crack closed) is obtained continuously throughout the experiment. In the initial stage, cantilever beam specimens were used in a manner similar to the flat specimen method. Soon it was realized that a different approach based on 'pure bending' would be more convenient. The proposed approach eliminated the base reaction and simplified the stress field in the specimen by removing a translational force. The schematic drawings of the 'pure bending' setup are in Figures 3.2 and 3.3. The whole vibrating H-assembly is suspended on flexible strings, so virtually no reactions are transferred to the base, and very small translational and tensile forces are invoked in the specimen (caused by the difference of the yoke masses and by specimen curvature during bending). This 'pure bending' setup was further developed and will be described in more detail here.

The fatigue crack growth rate methodology can take full advantage of the knowledge of the actual load and crack length of the specimen. Therefore, all classical modes of the fatigue crack growth experiment are possible, including constant amplitude, K-control mode, which includes load shedding and load increase, as well as the new 'rate-control' modes. The use of a particular mode can be related to the number of fatigue cycles N or the crack length a, and test segments with various control modes can be combined to automatically initiate and control the growth of the fatigue crack.

3.1.1 Excitation

To apply bending to the specimen, an H-shaped assembly formed by yokes and the sample is utilized (see Fig. 3.2). The sample is clamped into two equal yokes at its ends. The yokes are suspended to a rigid frame using

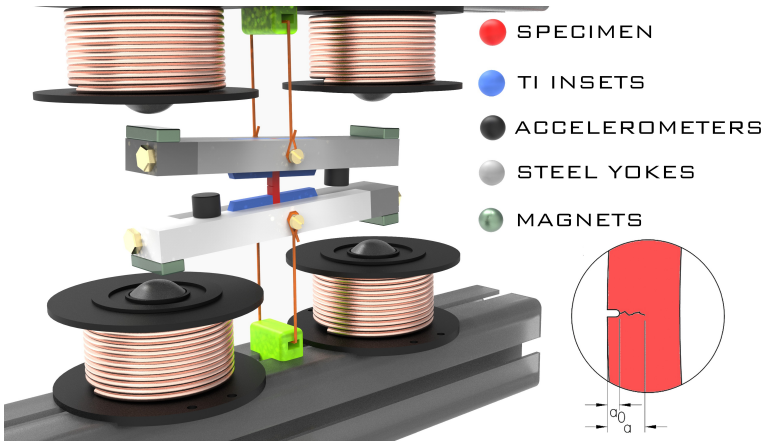

Figure 3.2: Schematic drawing of the resonance bending fatigue crack growth test apparatus.

Figure 3.3: The resonance bending fatigue crack growth test apparatus: left - standard setup, right - increased temperature setup.

flexible strings, so the position of the H-assembly is fixed in space. At the same time, the yokes can freely rotate in the suspension. The electromagnetic field of the coils acts on the magnets at the end of the yokes and introduces an excitation moment M_{e} that forces the system to vibrate. The vibration of the yokes at resonance then invokes the bending moment M_{t}, which is much higher than M_{e}. The value of the bending moment is given by the angular acceleration $\ddot{\alpha}$ of the yoke multiplied by the yoke moment of inertia J_y as

$$M_{\mathrm{t}} = \ddot{\alpha} J_y. \tag{3.1}$$

The excitation frequency is controlled by the phase locked loop technique; thus, resonance is easily obtained and maintained. The sample is excited, so the pure bending mode corresponding to the first bending mode shape can be obtained. Other vibration modes can occasionally be excited if the relevant harmonic condition is met. These modes can be avoided by selecting suitable yoke parameters or by modifying the test procedure. The motion of the yokes is sensed by accelerometers that output acceleration signals $a(t)$. The use of two accelerometers enables one to detect most of the parasitic vibration

modes, i.e., modes other than the desired pure bending mode. The bending mode signal $\ddot{\alpha}(t)$ can be easily discriminated in the two accelerometer setup. This signal is then utilized in the phase locked loop control of the excitation frequency, as well as in the control loop for the bending moment M_t, and is analyzed by the differential compliance method to obtain the crack length a.

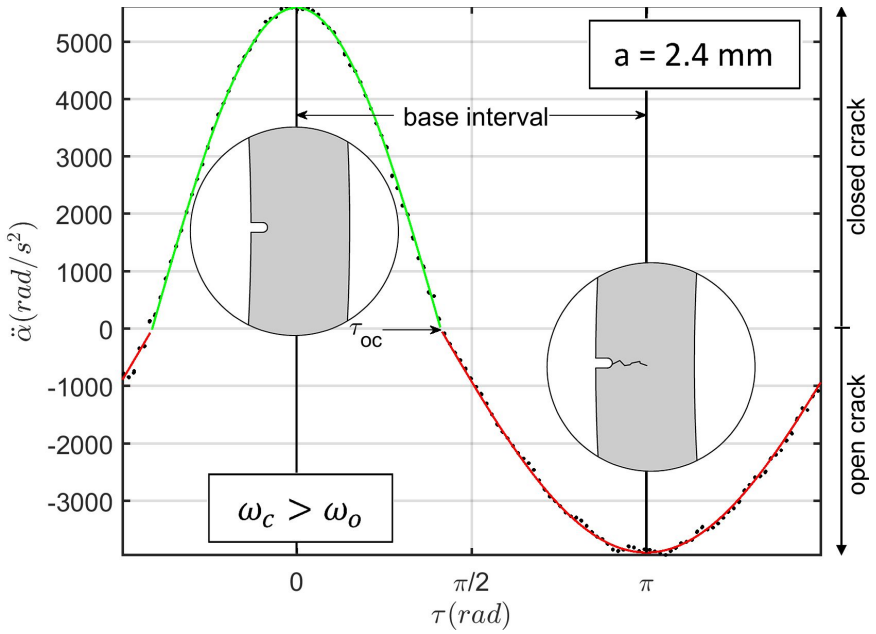

Figure 3.4: Typical waveform of the accelerometer output. The x axis corresponds to phase coordinate τ.

3.1.2 Crack length measurement

The differential compliance method evaluates the crack length a from the angular acceleration waveform $\ddot{\alpha}(t)$ (see Fig. 3.4) of a specimen with a breathing crack. The uncracked specimen would vibrate harmonically following the cos function. The effect of breathing crack is clearly indicated by the decrease in vibration frequency for the part of the waveform with an open crack (red curve in Fig. 3.4). The angular acceleration of the yokes is obtained from two accelerometer signals as $\ddot{\alpha}(t) = r_a \frac{a_u(t)+a_d(t)}{2}$. Here, r_a is the horizontal distance of the accelerometer from the center of the yoke; $a_u(t)$ and $a_d(t)$ represent the signals from the accelerometers mounted on the upper and lower yokes. The formula is valid for small rotational angles.

The compliance based methods are routinely used for the measurement of crack length during fracture toughness and fatigue crack growth rate tests. Under the assumption of linear elasti behavior, a precise crack length can be obtained. For standard test specimens, the relationship between crack length and specimen compliance is provided, e.g., in [82] for clip gages and [83] for back face strain gages. In these works, the crack length is computed using an inversion of a nondimensional compliance function. The concept of

nondimensional compliance $\Phi(a/h)$ describes the crack added compliance as a function of the crack length for specimens of a given shape but possibly differing in dimensions and elastic properties. The concept of nondimensional compliance will be utilized in the differential compliance method presented below.

Nondimensional Compliance

The transformation of the crack added compliance c_{crack} into crack length a is based on linear fracture mechanics (LFM), and its derivation for beam bending is described for the plane strain condition and small scale yielding, e.g., in [84]. Let us assume a rectangular specimen cross section with thickness b and width h. Applying a bending moment M_{t}, the crack induced compliance is represented by the additional rotation α_{crack} of the sample free ends (yokes). The crack added compliance is then $c_{\text{crack}} = \frac{\partial \alpha_{\text{crack}}}{\partial M_{\text{t}}}$. The Castigliano's principle states that the generalized displacement α_{crack} is the partial derivative of the strain energy U with respect to the generalized force M_{t}.

$$2\alpha_{\text{crack}} = \frac{\partial U}{\partial M_{\text{t}}}. \tag{3.2}$$

At the same time, strain energy can be expressed by integrating the elastic strain energy release rate G with respect to a:

$$U = b \int_0^{\text{a}} G da \tag{3.3}$$

Assuming plane strain and small scale yielding, the release rate G can be expressed as a function of the stress intensity factor and, hence, crack length as:

$$G = \left(1 - \nu^2\right) \frac{K_{\text{I}}^2}{E} = \frac{\left(1 - \nu^2\right)}{E} \sigma^2 a \pi f^2 \left(\frac{a}{h}\right), \tag{3.4}$$

where $f = f\left(a/h\right)$ is a standard shape function. In the following computation, the shape function of [85] was used for a beam subjected to pure bending. The remote bending stress σ is equal to the applied bending moment divided by the section modulus of the sample, as follows:

$$\sigma = \frac{6 M_{\text{t}}}{b h^2}. \tag{3.5}$$

Let us define the nondimensional compliance Φ as:

$$\Phi = \int_0^{\text{a}} \frac{a}{h} f^2 \left(\frac{a}{h}\right) da. \tag{3.6}$$

Let us compute the second moment of area of a rectangular beam as:

$$I = \frac{b h^3}{12}. \tag{3.7}$$

The crack added compliance can be obtained by plugging eq. 3.4 and eq. 3.6 into eq. 3.3 and differentiating it according to eq. 3.2 as:

$$c_{\text{crack}} = \frac{\partial \alpha_{\text{crack}}}{\partial M_{\text{t}}} = \frac{3\pi h \left(1-\nu^2\right) \Phi(a/h)}{EI} \tag{3.8}$$

Finally, the fracture mechanical crack length a can be expressed using an inverse of the non-dimensional compliance function Φ^{-1}:

$$a = h\Phi^{-1}\left(\frac{EIc_{\text{crack}}}{3\pi h\left(1-\nu^2\right)}\right). \tag{3.9}$$

The crack added compliance c_{crack} is a sum of compliance c_{n} added by the notch and compliance c_{bc} added by the breathing crack, i.e. $c_{\text{crack}} = c_{\text{n}} + c_{\text{bc}}$. The breathing crack compliance is equal to the difference in compliances of the specimen with open c_{o} and closed crack c_{c}, i.e., $c_{\text{bc}} = c_{\text{o}} - c_{\text{s}}$. The notch length a_{n} can be measured precisely before the test, and thus the notch added compliance c_{n} can be computed according to 3.8. Then the crack added compliance c_{crack} is equal to:

$$c_{\text{crack}} = c_{\text{bc}} + c_{\text{n}} = c_{\text{o}} - c_{\text{c}} + c_{\text{n}}, \quad c_{\text{n}} = \frac{3\pi h \left(1-\nu^2\right) \Phi(a_{\text{n}}/h)}{EI}. \tag{3.10}$$

It should be noted that eq. 3.9 is valid only when the influence of the notch on the stress intensity factor is small. That means that fatigue crack extension from the notch, i.e., the length of the breathing crack must be large enough compared to the notch end radius. An approximate formula describing the stress intensity factor of a crack growing from the notch is given, e.g., by Fett in [85] as:

$$K = K^* \tanh\left(2.243\sqrt{\frac{a-a_{\text{n}}}{R_n}}\right), \tag{3.11}$$

where R_n is the notch radius, K^* is the stress intensity factor of the fictitious crack of the same fracture mechanical length a in a specimen without a notch. It can be evaluated using the shape function $f(a/h)$ from [85] as:

$$K^* = \sigma f(a/h)\sqrt{\pi a}. \tag{3.12}$$

The influence of the notch with radius $R_n = 0.075\,\text{mm}$ decreases to $0.25\,\%$ for $a - a_{\text{n}} \geq 0.2\,\text{mm}$. Despite such a small influence, the correction equation 3.11 was incorporated into the solution by modifying the geometric function f in eq. 3.4 accordingly, in the hope of capturing the propagation of small fatigue cracks in the future.

Vibrational signal analysis

Both the applied load measurement and the crack length measurement depend on the parameters of the vibrational signal $\ddot{\alpha}(t)$. These parameters can be obtained by a simple numerical evaluation of vibrational signal extremes and zero crossings. However, due to the noise present in the signal, such evaluations will not offer sufficient precision and robustness, especially for low

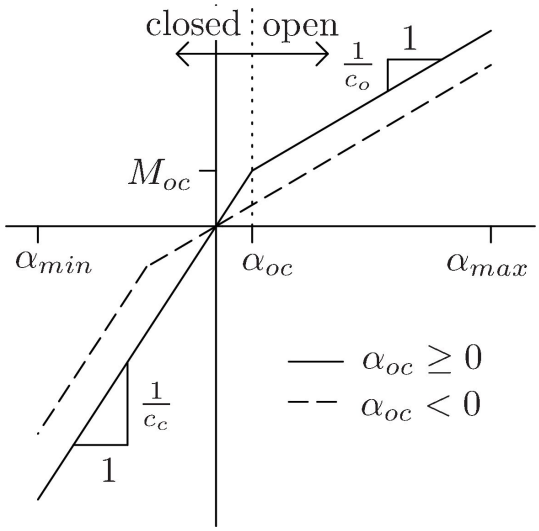

Figure 3.5: The bilinear spring characterization of sample stiffness. The solid line corresponds to $\alpha_{\mathrm{ac}} \geq 0$, the dashed line corresponds to $\alpha_{\mathrm{ac}} \geq 0$

crack propagation rates at low loads. In order to achieve a robust description of the vibrational waveform, a model function of the vibration system was derived. The derivation of the model, as well as the specific fitting procedure and the transformation of the parameters into the fatigue crack length a and the fatigue crack driving force $K_{\max}$, are described in this section.

To model angular acceleration, the equation of motion of the vibrating system was formulated assuming negligible specimen mass and yoke compliance. The specimen was characterized as a bilinear spring with compliances c_{c} and c_{o} corresponding to closed and open crack states. It was also assumed that the crack opens and closes at a single crack opening angle α_{oc} that corresponds to an applied bending moment $M_{\mathrm{t}} = M_{\mathrm{oc}}$. The crack was assumed to be open for $\alpha > \alpha_{\mathrm{oc}}$. The relation of the reaction moment M_{t} caused by angular deflection α is presented in figure 3.5. The reaction moment M_{t} is described as:

$$\begin{aligned} M_{\mathrm{t}} &= M_{\mathrm{oc}} + \tfrac{(\alpha-\alpha_{\mathrm{oc}})}{c_{\mathrm{o}}} \quad \text{for} \quad \alpha \geq \alpha_{\mathrm{oc}}, \\ M_{\mathrm{t}} &= M_{\mathrm{oc}} + \tfrac{(\alpha-\alpha_{\mathrm{oc}})}{c_{\mathrm{c}}} \quad \text{for} \quad \alpha < \alpha_{\mathrm{oc}}. \end{aligned} \tag{3.13}$$

The yoke is described by its moment of inertia J_y. The acceleration of the joke invokes the bending moment $M_{\mathrm{r}} = J_y\ddot{\alpha}$ acting on the specimen. It is assumed that the system damping is compensated by excitation, and these two terms cancel in the equation of motion. Then, the following nonhomogeneous ordinary differential equation describes the system:

$$J_y\ddot{\alpha} + M_{\mathrm{t}}(\alpha) = 0. \tag{3.14}$$

The value of the crack opening moment M_{oc} depends on the sign of the crack

opening angle α_{oc} as follows:

$$\begin{array}{lll} M_{\mathrm{oc}} = \frac{\alpha_{\mathrm{oc}}}{c_{\mathrm{o}}}, & \text{for} & \alpha_{\mathrm{oc}} \geq 0, \\ M_{\mathrm{oc}} = \frac{\alpha_{\mathrm{oc}}}{c_{\mathrm{c}}}, & \text{for} & \alpha_{\mathrm{oc}} < 0. \end{array} \tag{3.15}$$

Equation 3.14 is a nonhomogeneous (note the constant term in M_{t}; see eq. 3.13) second-order constant coefficient ordinary differential equation. The solutions α of equation 3.14 corresponding to the open crack and closed crack segments can be found using the method of undetermined coefficients [86]. Choosing a harmonic complementary function leads to the following angular velocities of the sample movement:

$$\begin{array}{ll} \omega_{\mathrm{o}}^2 = (J_y c_{\mathrm{o}})^{-1} & \text{for} \quad \alpha \geq \alpha_{\mathrm{oc}}, \\ \omega_{\mathrm{c}}^2 = (J_y c_{\mathrm{c}})^{-1} & \text{for} \quad \alpha < \alpha_{\mathrm{oc}}, \\ \omega_{\mathrm{c}}^2 = (J_y c_0)^{-1} & \text{for uncracked specimen.} \end{array} \tag{3.16}$$

The solution can be expressed in phase space that reflects the symmetry and periodicity of the modeled system. Let $\omega = 2\pi f$ be the angular velocity of the periodic function, then the phase space coordinate $\tau \in [0, \pi]$ is defined as:

$$\tau = \pi - \|(\pi - (\omega t + \varphi) \bmod 2\pi)\| \,. \tag{3.17}$$

The phase shift φ describes the phase difference controlled by the phase locked loop. When the loop is locked, $\varphi = 0$ and the maximum angular deflection $\alpha_{\max}$ corresponding to the open crack is achieved at $\tau = \pi$, and the minimum angular deflection corresponding to the closed crack occurs at $\tau = 0$ (see Fig. 3.4). Then, one may express the solution of equation 3.14 as:

$$\begin{array}{lll} \alpha = A_{\mathrm{o}} \cos\left(\frac{\omega_{\mathrm{o}}}{\omega}(\pi - \tau)\right) + \alpha_{\mathrm{oc}} c_{\mathrm{o}} \left(\frac{1}{c_{\mathrm{o}}} - \frac{1}{c_{\mathrm{c}}}\right) & \text{for} & \alpha \geq \alpha_{\mathrm{oc}} \wedge \alpha_{\mathrm{oc}} \geq 0, \\ \alpha = A_{\mathrm{c}} \cos\left(\frac{\omega_{\mathrm{c}}}{\omega}\tau\right) & \text{for} & \alpha < \alpha_{\mathrm{oc}} \wedge \alpha_{\mathrm{oc}} \geq 0, \\ \alpha = A_{\mathrm{o}} \cos\left(\frac{\omega_{\mathrm{o}}}{\omega}(\pi - \tau)\right) & \text{for} & \alpha \geq \alpha_{\mathrm{oc}} \wedge \alpha_{\mathrm{oc}} < 0, \\ \alpha = A_{\mathrm{c}} \cos\left(\frac{\omega_{\mathrm{c}}}{\omega}\tau\right) + \alpha_{\mathrm{oc}} c_{\mathrm{c}} \left(\frac{1}{c_{\mathrm{c}}} - \frac{1}{c_{\mathrm{o}}}\right) & \text{for} & \alpha < \alpha_{\mathrm{oc}} \wedge \alpha_{\mathrm{oc}} < 0. \end{array} \tag{3.18}$$

However, instead of the angular deflection α, the angular acceleration $\ddot{\alpha}(t)$ is measured during the experiment. The model acceleration can be obtained by double differentiation of the solution 3.18 of equation 3.14 with respect to time. The model of angular acceleration is thus:

$$\begin{array}{ll} \ddot{\alpha} = -A_{\mathrm{o}} \omega_{\mathrm{o}}^2 \cos\left(\frac{\omega_{\mathrm{o}}}{\omega}(\pi - \tau)\right) & \text{for} \quad \alpha \geq \alpha_{\mathrm{oc}}, \\ \ddot{\alpha} = -A_{\mathrm{c}} \omega_{\mathrm{c}}^2 \cos\left(\frac{\omega_{\mathrm{c}}}{\omega}\tau\right) & \text{for} \quad \alpha < \alpha_{\mathrm{oc}}. \end{array} \tag{3.19}$$

The model function in eq. 3.19 has the form $\ddot{\alpha} = \ddot{\alpha}\,(t, \omega, \varphi, A_{\mathrm{o}}, A_{\mathrm{c}}, \omega_{\mathrm{o}}, \omega_{\mathrm{c}}, \alpha_{\mathrm{oc}})$. Later, it will be shown that the number of parameters can be reduced, as ω and A_{c} depend on the other factors. The coefficients A_{o} and A_{c} are related through the elastic energy stored in the samples at the point of maximum and minimum angular deflections $\alpha_{\max}$ and $\alpha_{\min}$. The elastic energies of the fully deflected sample with the closed crack $E_{\mathrm{c}} = \int_0^{\alpha_{\min}} M_{\mathrm{t}} d\alpha$ and the open

crack $E_o = \int_0^{\alpha_{max}} M_t d\alpha$ can be obtained by integrating equation 3.13 as:

$$\left.\begin{aligned} E_c &= \frac{\alpha_{min}^2}{2c_c} \\ E_o &= \frac{\alpha_{max}^2}{2c_o} + \frac{\alpha_{oc}}{2}\left(2\alpha_{max} - 1\right)\left(\frac{1}{c_c} - \frac{1}{c_o}\right) \end{aligned}\right\} \quad \text{for} \quad \alpha_{oc} \geq 0,$$
$$\left.\begin{aligned} E_c &= \frac{\alpha_{min}^2}{2c_c} + \frac{\alpha_{oc}}{2}\left(2\alpha_{min} - 1\right)\left(\frac{1}{c_o} - \frac{1}{c_c}\right) \\ E_o &= \frac{\alpha_{max}^2}{2c_o} \end{aligned}\right\} \quad \text{for} \quad \alpha_{oc} < 0. \tag{3.20}$$

As the modeled system is conservative (it is assumed that energy losses are compensated by excitation), it follows that $E_o = E_c$, and therefore the deflection α_{min} (closed crack at $\tau = 0$) can be related to the sample deflection α_{max} (open crack at $\tau = \pi$). Substituting formulas for c_c and c_o from equation 3.16 into equation 3.18 and evaluating the equation for $\alpha = \alpha_{max}$ and $\alpha = \alpha_{min}$, that is, for $\tau = 0$ and $\tau = \pi$ one obtains:

$$\begin{aligned} A_c &= -\frac{1}{\omega_c \omega_o}\sqrt{A_o^2\omega_o^4 + \alpha_{oc}^2\omega_c^2\left(\omega_o^2 - \omega_c^2\right)} && \text{for} \quad \alpha_{oc} \geq 0, \\ A_c &= -\frac{\omega_o}{\omega_c^2}\sqrt{A_o^2\omega_c^2 + \alpha_{oc}^2\left(\omega_o^2 - \omega_c^2\right)} && \text{for} \quad \alpha_{oc} < 0. \end{aligned} \tag{3.21}$$

To simplify the fitting procedure, let us introduce the crack opening phase τ_{oc} in phase space. This allows us to explicitly distinguish between phases with open and closed cracks based on the phase τ of the periodic cycle. For $\tau \geq \tau_{oc}$, the crack is open; for $\tau < \tau_{oc}$, it is closed. The coefficients τ_{oc} as well as ω are dependent on other coefficients and can be evaluated as follows. The reaction moment caused by the bending of the sample is continuous at τ_{oc} (see 3.5). Thus, from equation 3.14, it follows that $\ddot{\alpha}$ is also continuous at τ_{oc}, and α is also continuous at τ_{oc}. Therefore, substituting τ_{oc} into equations 3.18 and 3.19 and relating α for open and closed cracks to τ_{oc} yields the following system of equations for the unknowns τ_{oc} and ω:

$$\begin{aligned} &A_o \cos\left(\tfrac{\omega_o}{\omega}\left(\pi - \tau_{oc}\right)\right) - A_c \cos\left(\tfrac{\omega_c}{\omega}\tau_{oc}\right) = -\alpha_{oc} c_o \left(\frac{1}{c_o} - \frac{1}{c_c}\right) && \text{for} \quad \alpha_{oc} \geq 0 \\ &A_o \cos\left(\tfrac{\omega_o}{\omega}\left(\pi - \tau_{oc}\right)\right) - A_c \cos\left(\tfrac{\omega_c}{\omega}\tau_{oc}\right) = \alpha_{oc} c_c \left(\frac{1}{c_c} - \frac{1}{c_o}\right) && \text{for} \quad \alpha_{oc} < 0 \\ &A_o\omega_o^2 \cos\left(\tfrac{\omega_o}{\omega}\left(\pi - \tau_{oc}\right)\right) - A_c\omega_c^2 \cos\left(\tfrac{\omega_c}{\omega}\tau_{oc}\right) = 0 && . \end{aligned} \tag{3.22}$$

Let us substitute $C_c = \cos\left(\tfrac{\omega_c}{\omega}\tau_{oc}\right)$ and $C_o = \cos\left(\tfrac{\omega_o}{\omega}\left(\pi - \tau_{oc}\right)\right)$ and solve the system of linear algebraic equations 3.22 for C_c and C_o. Then τ_{oc} and ω can be obtained by solving the following system of equations:

$$\begin{aligned} \tfrac{\omega_o}{\omega}\left(\pi - \tau_{oc}\right) &= \operatorname{acos}\left(C_o\right) \\ \tfrac{\omega_c}{\omega}\tau_{oc} &= \operatorname{acos}\left(C_c\right). \end{aligned} \tag{3.23}$$

The solution of the system of equations 3.23 is:

$$\left.\begin{aligned} \omega &= \pi\omega_o\omega_c\left(\omega_c \operatorname{acos}\left(\tfrac{\alpha_{oc}\omega_c^2}{A_o\omega_o^2}\right) + \omega_o \operatorname{acos}\left(\tfrac{\alpha_{oc}}{A_c}\right)\right)^{-1} \\ \tau_{oc} &= \tfrac{\omega}{\omega_c} \operatorname{acos}\left(\tfrac{\alpha_{oc}}{A_c}\right) \end{aligned}\right\} \quad \text{for} \quad \alpha_{oc} \geq 0$$
$$\left.\begin{aligned} \omega &= \pi\omega_o\omega_c\left(\omega_o \operatorname{acos}\left(\tfrac{\alpha_{oc}\omega_o^2}{A_c\omega_c^2}\right) + \omega_c \operatorname{acos}\left(\tfrac{\alpha_{oc}}{A_o}\right)\right)^{-1} \\ \tau_{oc} &= \tfrac{\omega}{\omega_c} \operatorname{acos}\left(\tfrac{\alpha_{oc}\omega_o^2}{A_c\omega_c^2}\right) \end{aligned}\right\} \quad \text{for} \quad \alpha_{oc} < 0 \tag{3.24}$$

Now, having evaluated A_c, ω, and τ_{oc}, the model function reduces to $\alpha = \alpha\left(t, \varphi, A_o, \omega_o, \omega_c, \alpha_{oc}\right)$. A constant C has to be added to the model function, as the charge amplifier of the accelerometer shifts the output signal so that the mean value over a sufficiently long time interval is zero; i.e., it removes the DC part but, at the same time, adds an amplifier output DC offset. The constant C can either be computed to zero the DC offset of the model function, or it can be fitted as a free parameter of the model. The fitting of C is preferred as it cancels the DC offset of the amplification chain. Thus, in the presented method, the model function has six coefficients to be fitted:

$$\ddot{\alpha} = \ddot{\alpha}\left(t, \varphi, A_o, \omega_o, \omega_c, \alpha_{oc}, C\right) \tag{3.25}$$

The individual steps to obtain state values $[N, a, K_{max}, \sigma_{max}]$ from an accelerometer signal $\ddot{\alpha}(t)$ data are as follows:

1. fit $\ddot{\alpha}(t)$ by a simple harmonic function using the method described in IEEE 1057 standard [78] i.e. $\ddot{\alpha} = A(\sin(\omega t + \varphi - \pi/2) + C$,
2. compute $\ddot{\alpha}_{min} = \min(\ddot{\alpha}(t))$ and $\ddot{\alpha}_{max} = \max(\ddot{\alpha}(t))$, then estimate the initial fit values $[A_o, \omega_o, \omega_c, \varphi, C, \alpha_{oc}]$:

$$\begin{aligned} A_o &= \ddot{\alpha}_{max}/\omega^2, \alpha_{oc} = 0 \\ \omega_o &= \omega\sqrt{|2\ddot{\alpha}_{min}/\left(\ddot{\alpha}_{max} - \ddot{\alpha}_{min}\right)|} \\ \omega_c &= \omega\sqrt{|2\ddot{\alpha}_{max}/\left(\ddot{\alpha}_{max} - \ddot{\alpha}_{min}\right)|}, \end{aligned} \tag{3.26}$$

3. fit the equation 3.25 to the accelerometer signal $\ddot{\alpha}(t)$ using the Levenberg-Marquardt algorithm [87] with preconditioning from eq. 3.26, and save the fitted parameters.
4. compute the crack length a using formula 3.9, A_c using eq. 3.19 , τ_{oc} and ω using eq. 3.22,
5. compute nominal stresses Tab. 3.1 using eq. 3.1 and 3.5, then use eq. 3.11 to compute the corresponding stress intensity factors.

σ_{max}	maximum stress
σ_{oc}	crack opening stress
σ_{min}	minimum stress
$\Delta\sigma = \sigma_{max} - \sigma_{min}$	stress range
$\Delta\sigma_{eff} = \sigma_{max} - \sigma_{oc}$	effective stress range

Table 3.1: List of used load characteristics of one loading cycle.

The fitted coefficients can be further processed; i.e., to obtain the adjusted compliance ratio (ACR) as defined in section X4 of the ASTM E647 standard [41]. The factor U_{ACR} can be evaluated from the known compliances c_c and c_o (eq. 3.16) as:

$$\Delta K_{ACR} = U_{ACR}\Delta K, \quad U_{ACR} = \frac{c_{o0}}{c_{s0}}\frac{c_s - c_{o0}}{c_o - c_{o0}}. \tag{3.27}$$

In the above equation, c_o is the specimen compliance with an open crack, and c_s is the secant compliance defined as:

$$c_s = \frac{\alpha_{max} - \alpha_{min}}{M_{t,max} - M_{t,min}}, \tag{3.28}$$

The compliances c_{c0} and c_{o0} describe the compliance of the uncracked specimen at the beginning of the fatigue test, with the notch in compression and tension. To some extent, the possible asymmetrical yoke grip compliance can be reflected in this manner. The necessary maximum and minimum angular deflection of the yokes α_{max} and α_{min} can be obtained from eq. 3.18 by using $\tau = \pi$ and $\tau = 0$. The corresponding reaction moments $M_{t,max}$ and $M_{t,min}$ can be obtained from eq. 3.13.

After the experiment, the saved state values are divided into an arbitrary number of intervals, and the data reduction procedure based on a linear piecewise fit is performed.

3.1.3 Test modes

The method offers classical load control modes, as well as a newly developed "rate control" mode to regulate the specimen load. An individual test consists of segments defined by the test modes and corresponding parameters.

Load control test modes. In the load control modes, the loading variable (typically σ_{max} or K_{max}) is controlled by changing the excitation signal amplitude using a PID loop. In this mode, classical constant amplitude testing at $\sigma_{max} = \text{const}$ is possible. Alternatively, the load may be related to the number of cycles N or the length of the crack a. A typical example is the K control mode, where the applied stress intensity factor is:

$$K_{max} = K_0 e^{C(a-a_0)} \tag{3.29}$$

The mode parameters are represented by the initial and final crack lengths a_0 and a_{end}, the initial stress intensity factor K_0, and the normalized gradient C (or the final stress intensity factor K_{end}).

Rate control test mode. Both constant amplitude and K-control modes can lead to non-propagating crack. Crack propagation can stop, e.g. due to the material nonhomogeneity or due to crack closure. This makes load increase testing in the near threshold range almost impossible for nonhomogeneous AM materials. Therefore, a new control mode was developed. This mode is called "rate control". It enables direct control of the crack growth rate $\frac{da}{dN}$. The setpoint for the fatigue growth rate is described as a function of $v(a)$ (or $v(N)$) following the exponential relation:

$$v(a) = v_0 e^{C(a-a_0)}, \tag{3.30}$$

The mode parameters are represented by the initial and final crack lengths a_0 and a_{end}, the initial crack propagation rate v_0, and the normalized gradient C (or final crack propagation rate factor v_{end}).

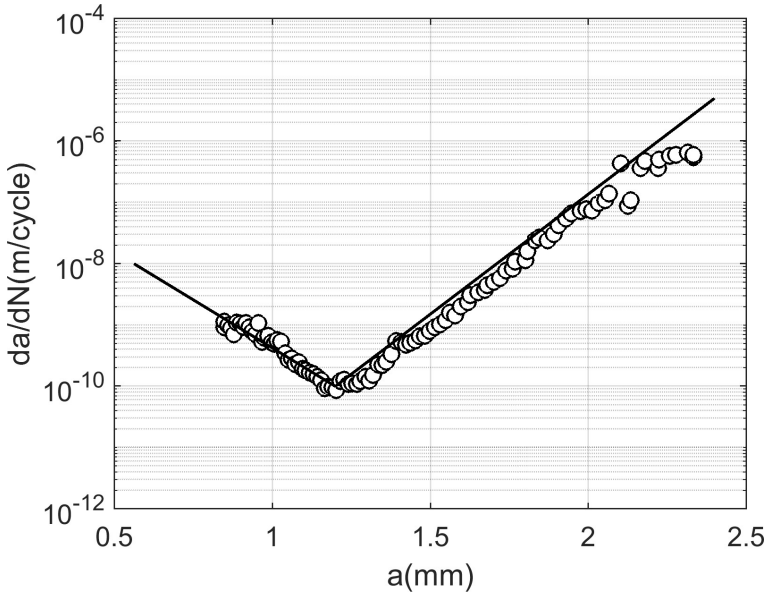

Figure 3.6: Relation of crack growth rate $\frac{\mathrm{d}a}{\mathrm{d}N}$ on crack length a during the rate controlled experiment with plasma sprayed tungsten (see [19]). The corresponding setpoint value $v(a)$ is shown as lines.

The controlled variable is the specimen load σ and the control loop tries to minimize the error e:

$$e = \left(\frac{\mathrm{d}a}{\mathrm{d}N} - v(a) \right)^2 . \tag{3.31}$$

The numerical derivative of the measured crack length $a(N)$, computed from the first order polynomial fit of the $a(N) = p_0 + p_1 N$ data, can be used to directly obtain $\frac{\mathrm{d}a}{\mathrm{d}N} \approx p_1$, provided the fitting interval length is adequate. That means several thousand datapoints are necessary for slow $\frac{\mathrm{d}a}{\mathrm{d}N} \approx 1 \times 10^{-11}\,\mathrm{m\,cycle^{-1}}$, whereas two datapoints are sufficient for high crack growth rates $\frac{\mathrm{d}a}{\mathrm{d}N} \approx 1 \times 10^{-6}\,\mathrm{m\,cycle^{-1}}$. Therefore, an adaptive selection of the fitting interval was implemented based on the indicated $\frac{\mathrm{d}a}{\mathrm{d}N}$ value.

Another inherent advantage of the rate control method is that the total number of cycles per segment N_{seq} is known. It can be obtained by integrating $\frac{\mathrm{d}N}{\mathrm{d}a}$ from eq. 3.30 as:

$$N_{\mathrm{seq}} = \frac{1}{C v_0} \left(e^{C(a_{\mathrm{end}} - a_0)} - 1 \right), \tag{3.32}$$

where a_{end} is the final crack length for the particular segment.

3.1.4 Fatigue test protocol

Typically, the test protocol should initiate the crack, extend it from the stress field of the notch, and then perform the fatigue crack growth rate measurement at increasing or decreasing loads. Many different approaches were tested, with the four segment protocol in Tab. 3.2 being used for most

seg.	a_0 (mm)	a_{end} (mm)	N_{seg} (cycles)	mode	formula
1	0.5	0.7	∞	load	$\sigma_{\max} = \sigma_0 \frac{N+10^6}{10^6}$
2	0.7	0.8*	$< 10^6$	load	$K_{\max} = K_{\max}(0.7)e^{-11(a-0.7)}$
3	0.8*	1.1	$\sim 11.7 \times 10^6$	rate	$\frac{da}{dN} = 10^{-10}e^{-7.67(a-0.8)}$
4	1.1	2	$\sim 7.8 \times 10^6$	rate	$\frac{da}{dN} = 10^{-11}e^{12.79(a-1.1)}$

* In case the crack stops propagation in segment 2, the starting crack length of segment 3 and its coefficient C (see eq. 3.30) is updated accordingly.

Table 3.2: Typical four segment protocol of the fatigue test. The number of cycles in a segment is limited in step 2, whereas in steps 3 and 4 the number of cycles is apriori known.

experiments. In segment 1, the load increases slowly until the crack extends by 0.2 mm. Very fast crack growth can follow crack initiation; therefore, very steep load shedding takes place in segment 2. The crack propagation may stop in segment 2; therefore, the length of the segment is limited to 10^6 cycles. At the end of segment 2, the crack has extended at least 0.2 mm from the notch, and the load is close to the threshold value. The crack is further grown in rate controlled load shedding to reach 1×10^{-11} m cycle^{-1} at a crack length of $a = 1.1$ mm. There, the actual fatigue crack growth rate test starts with $\frac{da}{dN}$ increasing to 1×10^{-6} m cycle^{-1} at $a = 2.0$ mm. The typical course of the experiment during rate controlled segments is shown in Fig. 3.6.

3.1.5 Validation of the testing method

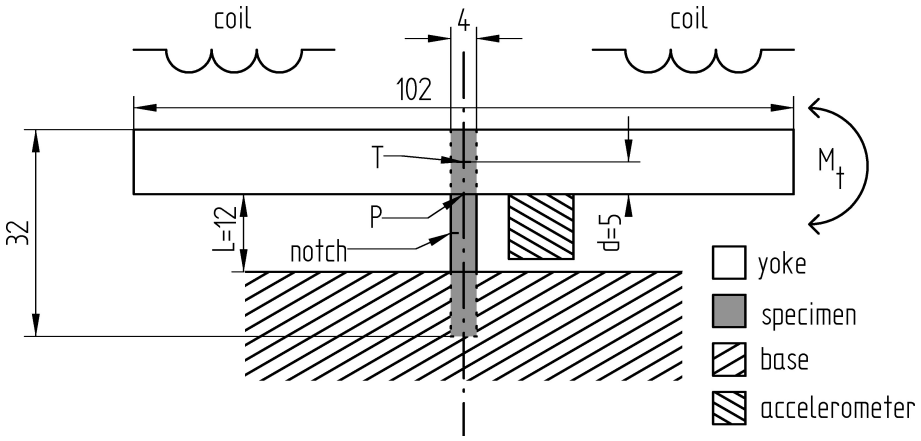

Figure 3.7: The cantilever bending setup used in the early phases of the FCGR setup design.

The basic validation of the fatigue crack growth measurement method was performed in [18] for 7075 aluminum alloy and 4340 steel loaded as cantilevers (see Fig. 3.7). Crack length measurement was validated using fractographic marks, while the data $\frac{da}{dN}$ were compared with the reference works [88, 89]. The fatigue crack length measurement using 'pure bending' symmetrical setup

was validated for 7075 aluminum alloy in [19]. Additional validation for the 2024 aluminum alloy was also performed (see Fig. 3.9). Some details of the validation not included in [19] are presented in this chapter. Several samples of 7075 aluminum alloy were fractographically marked by changing $K_{\max}$ at the selected indicated crack lengths, similarly to [18], but with a smaller distance between the marks (see Fig. 3.8). The fractographic crack length a_{f} was obtained by observing the fracture surface in a scanning electron microscope and digitizing the crack fronts using the SEM stage. The a_{f} value corresponding to a particular mark was obtained following the ASTM E399 standard [90].

The comparison of fractographically obtained crack length a_{f} and crack length a, indicated by the differential compliance method, is shown in Fig. 3.9. The fractographic crack length a_{f} was about 70 µm longer than the indicated crack length a.

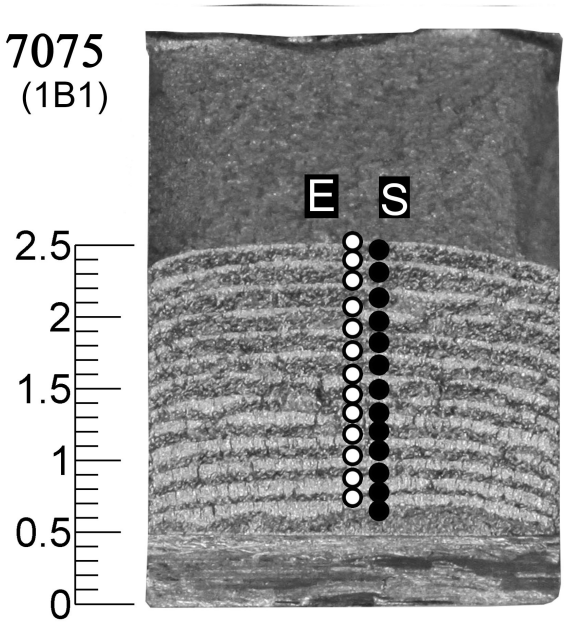

Figure 3.8: Fatigue marking on 7075-T651 specimen obtained by periodically varying $K_{\max}$. Marks S are at the starts of regions with $K_{\max} = 7\mathrm{MPa}\sqrt{\mathrm{m}}$ and marks E at the beginning of regions with $K_{\max} = 4\mathrm{MPa}\sqrt{\mathrm{m}}$.

Finite element model. In order to explain the observed difference in fractographic and indicated crack lengths, a finite element model was formulated reflecting the 3D nature of the problem, including the crack front shape. The crack front was described by a second order polynomial fitted to the crack front shapes of several specimens. Let x be the perpendicular distance of a crack front point from the specimen centerline. Then, using the formula from [91] and fitting it to the crack front data, one obtains:

$$a(x) = a(0) - 121\left(\max\left(x, 0.1h\right)\right)^2. \tag{3.33}$$

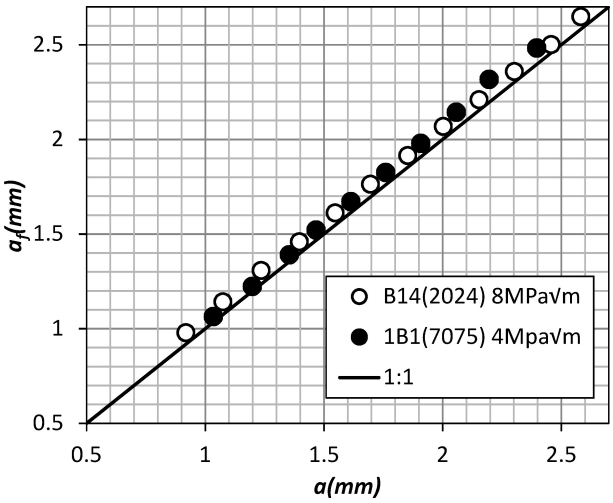

Figure 3.9: Comparison of real crack lengths a_f obtained fractographically with crack lengths estimated using the differential compliance method.

The 3D FEM modeled crack added compliance c_{crack} was transformed to nondimensional compliance Φ using eq. 3.8. This nondimensional compliance Φ is presented in Fig. 3.10 for curved and straight crack fronts and is compared to the 2D FEM and LFM formulas from eq. 3.6. The results of the fractographic analysis are presented using a nondimensional compliance plot Φ indicated during the marking test and the corresponding crack length a obtained through fractographic analysis.

It is clearly shown in Fig. 3.10 that LFM solution and straight crack front FEA data correlate very well. The fractographic data show slightly lower Φ values that, however, correspond closely to the FEM data of the curved crack front. Therefore, nondimensional compliance based on curved crack front FEM was used for experiments in the following studies [19, 21–24].

3.1.6 Peculiarities of the method

The fatigue crack growth methods described above differ from the classical fatigue crack growth rate methods in several aspects.

Notch stress field: The effect of the notch stress field is reflected by the correction factor of Fett (see [85], eq. 3.11). The stress intensity factor will increase significantly for the first 100 µm until it reaches the nominal value defined by the crack length a, see Fig. 3.11. This increase complicates the rate control mode for very short cracks and calls for more conventional methods of small crack testing, such as constant amplitude. The fatigue crack growth rate test is performed at a sufficient distance from the notch to make its effect negligible, as follows from eq. 3.11.

Plastic zone size: The sizes of both monotonic and cyclic plastic zones have a significant effect on the loading of the crack tip and the damping of the specimen. The presented methodology was based on the small scale yield

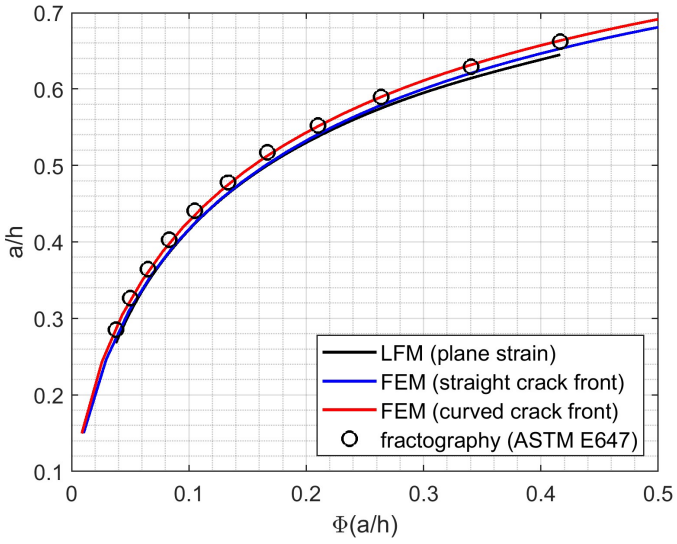

Figure 3.10: The nondimensional compliance function Φ related to crack length a. LFM and FEM - a postulated, Φ computed using 2D LFM and 3D FEA from assuming straight or curved crack front. Fractography - a obtained fractographically, Φ measured

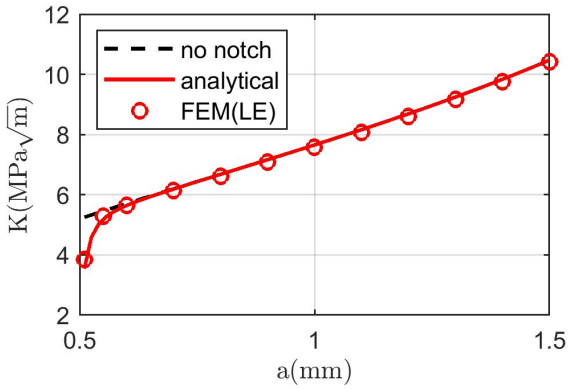

Figure 3.11: The stress intensity factor at loading moment M_t =1 N m obtained by the formula 3.11 and verified by 2D linear elastic FEM analysis for notch length a_0 =0.5 mm.

assumption; therefore, the plastic zone size limits the maximum value of the stress intensity factor for the valid fatigue crack growth rate test according to the ASTM E647 [41] standard. For an excentric loaded single notched specimen, the following formula must be fulfilled:

$$K_{\max} < \sigma_{\mathrm{fs}} \sqrt{\frac{\pi(h-a)}{4}} \sigma_{\mathrm{ys}} \tag{3.34}$$

Here, σ_{fs} represents the yield stress $R_{\mathrm{p0.2}}$ for low strain hardening materials with $R_m/R_{\mathrm{p0.2}} < 1.3$. For the high strain hardening materials, σ_{fs} represents

the flow strength $\frac{R_{p0.2}+R_m}{2}$. When the highest stress intensity factor is reached at the end of the fatigue experiment, the remaining ligament size is $h - a = 2\,\mathrm{mm}$, see Tab. 3.2. The corresponding upper load limit is then $K_{\max} > 0.04\sigma_{ys}$. For example, the 1050 aluminium with $R_{p0.2}$ calls for $K_{\max} < 4.4\,\mathrm{MPa}\sqrt{\mathrm{m}}$.

The amount of energy dissipated in the cyclic plastic zone also indicates its size. For example, during experiments with the above mentioned 1050 alloy, the specimen will dissipate all energy supplied at $K_{\max} \approx 4.7\,\mathrm{MPa}\sqrt{\mathrm{m}}$, and no further load increase will be possible. Therefore, modification of the setup to reach higher loads seems unnecessary, as the load limit approximately corresponds to the plastic zone limit of the ASTM E647 standard. Another example is shown in Fig. 3.13, indicating the load limit of the present setup and the resulting maximum crack propagation rate for 4330 steel. Rates approaching $5 \times 10^{-6}\,\mathrm{m\,cycle^{-1}}$ can be reached for materials with low damping and low crack propagation resistance. Thus, the method allows for the study of the near threshold and Paris regime, whereas the part of the $\frac{\mathrm{d}a}{\mathrm{d}N}(\Delta K)$ curve approaching dynamic fracture toughness must be measured by other methods.

The effect of σ_{tip}: The unknown residual stresses in the crack process zone, as well as the applied stress σ_{tip} (see, e.g., [92]), experienced by the process zone material during the negative part of the cycle, may play an important role, especially for shorter cracks. An experiment with 4340 steel was performed to assess the effect of σ_{tip}. The 2D linear elastic FEM method was used to evaluate σ_{tip} stress in the sample cross-section (see Fig. 3.12 for a case with a notch of length 0.5 mm. It is apparent that the influence range of the notch is limited and that the effect of the notch is negligible at $a > 1.1\,\mathrm{mm}$.

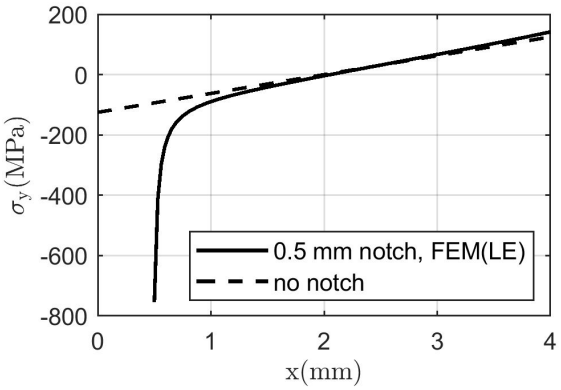

Figure 3.12: The stress $\sigma_{\mathrm{tip}} = \sigma_y$ applied in the compressive part of the loading cycle, 2D FEM data.

Stress ratio: The resonant nature of the presented method results in a negative stress ratio. During the test, the crack induced stiffness decreases the nominal stress in the positive (tensile) part of the loading cycle (see Fig.

3.4). During the compressive part (negative), the stiffness of the specimen, and hence, the nominal stress retains its value. Therefore, considering the relationship of the bending moment to stiffness according to eq. 3.13 and assuming a conservative system as in eq. 3.20, it follows that $M_t(0)$ is lower than $-M_t(\pi)$ and thus $R < -1$. In fact, R will decrease from $R = -1$ at the beginning of the experiment to $R \sim -1.4$ at $a = 2\,\mathrm{mm}$. There are two straightforward approaches to this problem:

1. follow the ASTM E647 recommendation and only use the positive part of the loading cycle, i.e., $K_{\max}$ as the crack driving force,

2. use ΔK_{eff} or ΔK_{ACR} as a crack driving force.

As discussed in [37], the assumption $\Delta K = K_{\max}$ corresponds to the stress ratio $R = 0$. Despite the negative nominal R, the crack tip experiences relatively low compressive stress. As described in the previous paragraph, the stress σ_{tip} during the evaluated part of the test, i.e., for $1\,\mathrm{mm} < a < 2\,\mathrm{mm}$ is low. In this range of a, compressive stress is concentrated in the crack mouth area, and the area close to the neutral axis receives a significantly lower load. Therefore, the material around the crack tip experiences a load ratio similar to that of remote loading with $R = 0$. This partly justifies the above assumptions and enables one to roughly compare the obtained $\frac{\mathrm{d}a}{\mathrm{d}N}(\Delta K)$ data with the results of conventional tests with low positive stress ratios. Fig. 3.13 illustrates that $\frac{\mathrm{d}a}{\mathrm{d}N}(\Delta K)$ data obtained for 4330 high strength steel can be compared with $R = 0.1$ data of 4330 steel from [93] and 4340 steel from [94].

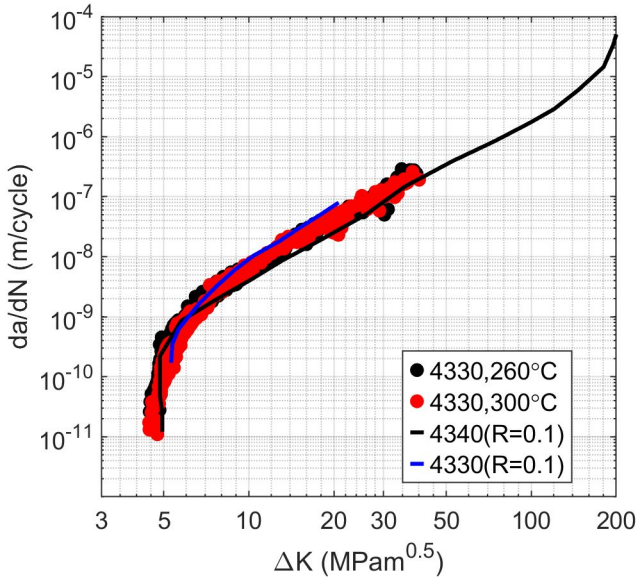

Figure 3.13: Fatigue crack growth rate of AISI 4330 high strength steel at two tempers compared with 4330 and 4340 reference data.

3.1.7 Fatigue crack growth rate data model

It is desirable to describe the $\frac{\mathrm{d}a}{\mathrm{d}N}$ data obtained during the fatigue crack growth rate test using a suitable parametric model to simplify the evaluation and discussion of the obtained data. Many different models can be used, including the formulas of Paris, Klesnil-Lukas, and different versions of the Forman type equation. It is beyond the scope of this work to describe these models, and the reader is directed to the review paper of Schwalbe [95]. From all the models available, the Hartmann-Schijve (H-S) variant of the Forman equation was selected for its simplicity and ability to fit all three stages of fatigue crack growth, i.e., the near threshold, Paris, and cyclic fracture toughness regimes.

The H-S model is based on the Paris type formula.

$$\frac{\mathrm{d}a}{\mathrm{d}N} = D\Delta\kappa^p. \tag{3.35}$$

Here $\Delta\kappa$ is Schwalbe's crack driving force defined as:.

$$\kappa = \frac{\Delta K - \Delta K_{\mathrm{thr}}}{\sqrt{1 - \frac{K_{\max}}{A}}}. \tag{3.36}$$

Here A is cyclic fracture toughness, and ΔK_{thr} is the value approached by the stress intensity factor range at the fatigue crack growth rate threshold. Note that ASTM E647 [41] defines another threshold value ΔK_{th} corresponding to $\frac{\mathrm{d}a}{\mathrm{d}N} = 1 \times 10^{-10}\,\mathrm{m\,cycle^{-1}}$.

The use of the H-S formula to fit various FCGR data, including small specimens, was pioneered by Jones et al. [28–31] who used direct nonlinear fitting methods. To obtain a robust fit, we have developed a new fitting methodology and applied it to tungsten and its alloys in [33].

The fitting method was based on the fitting of the inverse function $K\left(\frac{\mathrm{d}a}{\mathrm{d}N}\right)$. In order to invert the H-S formulas in eq. 3.35 and 3.36, only positive values of stress intensity factors $K_{\max}$, ΔK, and the Schwalbe's crack driving force $\Delta\kappa$ are considered:

$$K_{\max} > 0, \Delta K > 0, \Delta\kappa > 0. \tag{3.37}$$

For the stress ratio R, it holds:

$$\Delta K = K_{\max}(1 - R), \tag{3.38}$$

therefore eq. 3.36 transforms to:

$$\Delta\kappa = \frac{K_{\max}(1 - R) - \Delta K_{\mathrm{th}}}{\sqrt{1 - \frac{K_{\max}}{A}}}. \tag{3.39}$$

As noted in eq 3.37, $\Delta\kappa$ must be positive. At the same time, the denominator of eq. 3.39 must be real. Therefore:

$$K_{\max} < A \wedge K_{\max} > \frac{K_{\mathrm{th}}}{1 - R} \tag{3.40}$$

Note that the value of $\Delta\kappa$ outside the interval defined by eq. 3.40 is undefined; thus, the error of the fit $\frac{\mathrm{d}a}{\mathrm{d}N}$ cannot be computed for these data points. Moreover, the model function has very high gradients near K_{th} and A, further complicating the fit. Therefore, the inverse fitting procedure was adopted. Fortunately, both eq. 3.35 and eq. refeq:Schwalbe can be inverted:

$$\Delta\kappa = \left(\frac{1}{D}\frac{\mathrm{d}a}{\mathrm{d}N}\right)^{\frac{1}{m}},$$

$$\begin{aligned} K_{\max} =& \frac{\Delta\kappa}{2A\left(R^2-2R+1\right)}\Big(\sqrt{4A\left(\Delta K_{\mathrm{thr}}\left(R-1\right)\right)+A\left(R^2-2R+1\right)+\kappa^2} \\ & -\kappa^2+2AK_{\mathrm{th}}\left(1-R\right)\Big). \end{aligned} \tag{3.41}$$

Fitting eq. 3.41 to experimental data can be done by any nonlinear iterative technique (e.g., by the trust region reflective algorithm [96]), as the domain of the independent variable $\frac{\mathrm{d}a}{\mathrm{d}N}$ is only limited by the part of eq. 3.41 below the radical:

$$4A\left(\Delta K_{\mathrm{thr}}\left(1-R\right)-A\left(R^2-2R+1\right)\right)<\kappa^2, \tag{3.42}$$

This condition is often fulfilled, as $\Delta K_{\mathrm{thr}}\left(1-R\right)-A\left(R^2-2R+1\right)$ is always negative for $R=-1$. For $R=0.1$, it is sufficient to have $A\geq 1.1K_{\mathrm{th}}$; for $R<0.8$, it must hold that $A\geq 5K_{\mathrm{th}}$. For higher R values, imposing bounds on K_{thr} or A may be desirable.

The fatigue crack growth data obtained for small specimens will usually not allow us to fit the dynamic fracture toughness A as there are rarely any data with $\frac{\mathrm{d}a}{\mathrm{d}N}>10^{-6}$m/cycle available. Therefore, static fracture toughness K_{IC} measured after the FCGR test can be used to provide a very rough approximation of dynamic fracture toughness A, i.e., $A\sim K_{\mathrm{IC}}$ can be assumed.

The fitting procedure was implemented as a Matlab routine `HS_CTU.m` and made available online in the paper [33].

3.2 Fracture toughness

Fracture toughness K_{IC} represents a very important engineering fracture property of the material. Moreover, as discussed in the previous section, it provides a rough estimate of the cyclic fracture toughness A necessary for the H-S description of the FCGR data. Therefore, a method for measuring fracture toughness was implemented. A detailed description of the method is provided in a paper [24]. The availability of specimens after the fatigue test enables two approaches to the measurement of K_{IC}. Fracture toughness measured after the standard FCGR test ending at $\frac{\mathrm{d}a}{\mathrm{d}N}=1\times10^{-6}\,\mathrm{m\,cycle^{-1}}$ will approximate dynamic fracture toughness A as the crack tip has experienced a significant cyclic load. At the same time, fracture toughness K_{IC} obtained

from sharp pre-crack precycled at very low $\frac{da}{dN} = 10^{-10}$m/cycle will represent the standardized quasi-static fracture toughness. Both approaches use the following procedure for measuring fracture toughness based on the ASTM E1820 standard [65].

The fracture toughness was measured in a three-point bending fixture (see Fig. 3.14) with a span of L=27 mm using the Hegewaldt-Peschke Inspekt 100 testing machine with 1 kN or 20 kN force transducer. Due to the small size of the loading fixture, no rollers were used, and the specimen contacts were fixed cylinders with a diameter of 4 mm. The contact points of the fixture were lubricated in order to reduce longitudinal stress in the specimen. The loadline displacement was measured by an LVDT sensor. The span to specimen with ratio was $L/h = 6.75$, which differs significantly from the ratio $L/h = 4$ recommended by the standard. Therefore, the necessary specimen compliance was calculated following the formulas of Guinea [97]. The experiment was performed under deflection control with a crosshead speed of $\dot{u} = 1 \times 10^{-6}\,\mathrm{m\,s^{-1}}$ to $2.5 \times 10^{-6}\,\mathrm{m\,s^{-1}}$. Digital image correlation (DIC) was used to measure crack mouth opening displacement (COD) and crack length a. For brittle specimens, the convolution based method of displacement field evaluation [9] was used to establish the crack length at the surface of the specimen. For ductile materials, the crack length was measured using a standard unloading compliance method. Resistance curves based on loadline displacement u and COD were evaluated to obtain $J_{\mathrm{IC,u}}$ and $J_{\mathrm{IC,COD}}$ values. These values were also converted to fracture toughness using the plane deformation formula $K_{\mathrm{IC}} = \sqrt{\frac{J_{\mathrm{IC}}E}{1-\nu^2}}$.

3.3 Stress-strain

The Stress-strain properties of the tested materials are of interest in themselves, but at the same time, they are crucial for the evaluation of the fracture toughness experiment and for the measurement of the crack length by compliance. The simple specimen geometry used does not allow conventional tensile testing to be performed, as there are no provisions for sample gripping. Thus, the stress-strain behavior was measured under four-point bending using a method suggested by Herbert [64]. The method relies on precise strain measurements on the tensile and compressive faces of the bent beam. Unfortunately, at the time of publication at the beginning of last century, there were no suitable measurement methods available. With the discovery of strain gages, such measurements have become possible and have provided data comparable to the uniaxial test (see [98]). The development of digital image correlation (DIC) further simplified the measurement, and the method was adopted as described in a paper [24]. Under the assumption of a homogeneous specimen, the method enabled the evaluation of tensile and compressive stress-strain curves up to a material deformation of 5 %.

The specimens without notches were loaded in a four-point bending setup using a special fixture (see Fig. 3.14) with an outer span of $L = 27\,\mathrm{mm}$

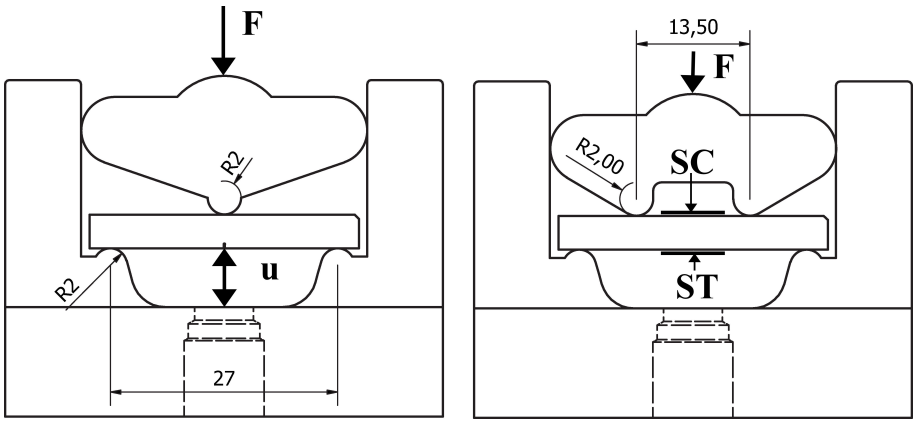

Figure 3.14: Geometry of fixtures for 3pb fracture toughness and 4pb stress-strain measurement [20]. SC and ST denotes position of compressive and tensile strain gages used on some specimens. u is the loadline displacement.

and an inner span of $l = L/2$. Inspekt 100 testing machine (Hegewaldt-Peschke, Nossen, Germany) with 1 kN or 20 kN force transducer was used in displacement control mode with a crosshead speed of $\dot{u} = 1 \times 10^{-6}\,\mathrm{m\,s^{-1}}$ to $5 \times 10^{-6}\,\mathrm{m\,s^{-1}}$. If the specimen did not fail, the loading was stopped at a deflection corresponding to the tensile deformation of the specimen surface $\varepsilon_t \sim 3 - 5\%$. The complete displacement field obtained by the DIC system (see [24]) was fitted using the plane strain analytical formula, and the surface strain values on the tensile and compressive surfaces of the specimens ε_t and ε_c were extrapolated from the fit. The corresponding stresses were computed from the bending moment M, surface deformations ε_t and ε_c as:

$$\sigma_\alpha = \frac{dM\,(\varepsilon_c + \varepsilon_t) + 2M\,(d\varepsilon_c + d\varepsilon_t)}{bh^2 d\varepsilon_\alpha}; \quad \alpha = c, t. \tag{3.43}$$

The numerical differences dM, $d\varepsilon_c$, and $d\varepsilon_t$ were calculated using a four-point central difference formula. The method worked well for specimens with a continuous displacement field. However, some materials exhibited cracking in the tension part of the specimen, making the data with higher deformation invalid.

3.4 Results

This section summarizes the results of small specimen testing presented in papers [18–39]. Namely, the papers include conventional 7075 aluminum alloy and 4340 steel [18], plasma sprayed refractory W and Mo [19, 23], tungsten heavy alloys [33] and metallic glasses [32], powder metallurgy sintered and forged tungsten heavy alloys [23], cold sprayed pure metals [21, 24], 316 steel [22], diamond based MMC's [25] (awarded JTST best paper [40]), Ti6Al4V [27], pure Al [36], cold sprayed and thermomechanically processed Aluminum 6061 alloy [38] and finally directed energy deposited Inconel 738LC [35] and Inconel 718 [39] superalloys.

3.4.1 Plasma spray

W based deposits

After evaluating the basic methodology of the fatigue crack growth rate test for 7075 aluminum alloy and 4340 steel, the method was applied to assess the fatigue crack growth rate in plasma sprayed refractories in [19]. In this research, the symmetrical 'pure bending' setup was used for the first time, vibration analysis was extended with fatigue crack opening stress σ_{oc} and the rate control mode was introduced. It immediately appeared that the measurement of σ_{oc} is very important as it indicated that for W deposit the cracks remain open throughout the majority of the loading cycle. Therefore, it was necessary to preload the sample mechanically, so that the crack opening can be detected and the reference compliance measured.

The results of further plasma sprayed W deposits testing that complement the original paper [19] were published in [23]. In this study, stress-strain and fracture toughness were measured from the same bending specimen geometry. New W deposits were prepared from finer powder than in [19]. These deposits had a much lower porosity than the coarse powder deposits in [19]. As a result of reduced porosity, the fatigue crack growth resistance at low crack propagation speeds was significantly higher. However, the porous deposit had a higher fracture toughness K_{IC} with values that resembled powder metallurgy tungsten. The globular nature of the porosity of the coarse W deposit and its high oxygen content might be the causes of the observed behavior. The powder metallurgy W sheet was used as a reference material in this study; however, attempts to initiate and grow a fatigue crack in a stable manner failed. The material fractured immediately, when the fatigue crack was initiated. In order to reach stable fatigue crack growth, elevated temperature tests were performed. It was shown that higher cyclic fracture toughness may be obtained for powder metallurgy W above 130 °C, but no stable fatigue crack growth was achieved up to 150 °C.

Other papers focused on W based heavy alloys (WHA), a composite material with W particles embedded in a NiW solid solution matrix, often containing other elements to promote W solubility. In [20], WHA produced

by the powder metallurgy route were tested in both sintered/quenched state and after rotary swaging/annealing. After swaging/annealing, stress-strain tests showed a significant increase in yield strength $R_{p0.2}$ and the FCGR test indicated a higher crack growth resistance. However, fracture toughness K_{IC} was significantly reduced. Instrumented indentation was applied to ascertain the local effect of rotary swaging on both constituents of the WHA, i.e. on the W particles and Ni based matrix. It was observed that the increase of instrumented Vickers hardness HVM at high loads is more intensive than at low loads. For high loads, the probed volume is larger than the characteristic particle size. For low loads, the probed volume is largely limited to the interior of the particle or the matrix. The synergetic effect of particle and matrix hardening was suspected in the paper, and later debates suggest that the change of the hardness should be considered at or close to the particle/matrix interface because of thermo-mechanical action of the swaging. At the same time, compressive residual stress of the W particles was measured by XRD, however, without a corresponding tensile stress in the Ni rich matrix.

WHAs manufactured by RF-plasma deposition from mechanically mixed powders were investigated in [34]. It was shown that a fully developed WHA structure can be obtained by plasma spray. The mechanical and fracture properties were approaching the qualities of WHA manufactured by the powder metallurgy route. The quantification of the $\frac{\mathrm{d}a}{\mathrm{d}N}$ data required a suitable model equation that can be easily fitted to the wide range of experimental data. The Hartman-Schijve equation fitting methodology described in section 3.1.7 was developed and applied to the available W and WHA data in [33], see Figure 3.15.

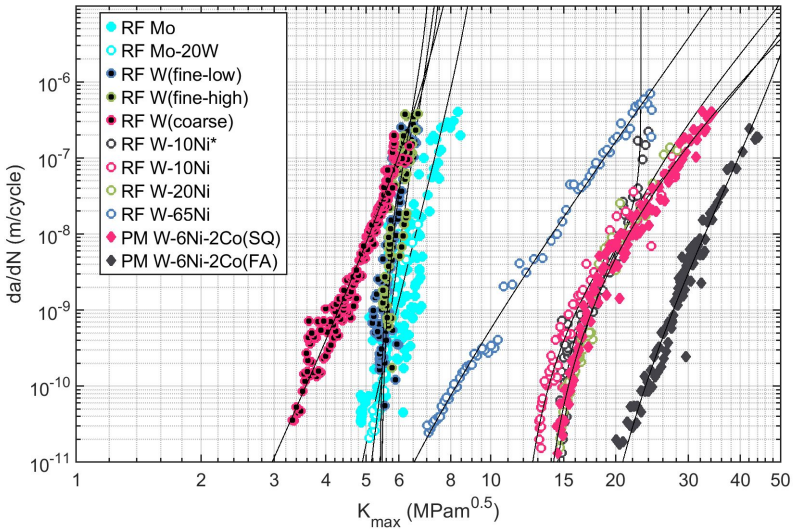

Figure 3.15: FCGR data of investigated refractory materials from [33].

Metallic glasses

Another plasma sprayed material under investigation were the plasma sprayed metallic glasses (see [32]), namely :

$Fe_{56.04}Co_{13.45}Nb_{5.5}B_{25}$	denoted as FeCoNb,
$(Fe_{0.9}Co_{0.1})_{76}Mo_4(P_{0.45}C_{0.2}B_{0.2}Si_{0.15})_{20}$	denoted as FeCoMo.

The FeCoMo glass had a high glossy phase amount of 92%, whereas FeCoNb only contained 53% amorphous phase by weight. The highly amorphous FeCoMo showed lower crack growth resistance for both quasi-static and fatigue loading. In FeCoNb, unbonded splat interfaces were indicated by the large difference in elastic moduli in tension and compression. Relatively high fracture toughness of $3.9 \pm 0.8\text{MPa}\sqrt{\text{m}}$ for FeCoMo and $8.1 \pm 2.2\text{MPa}\sqrt{\text{m}}$ for FeCoNb. To explain this behavior, we hypothesized that the crystal phase and the related porosity acted as crack propagation barriers by releasing the crack tip strain. A similar mechanism for coarse grained W was also suggested in our previous work [19, 23].

3.4.2 Cold spray

Pure Al, Cu, Ti and Ni

The full range of mechanical and fracture tests was performed on cold sprayed Al, Cu, Ti, and Ni pure metals in the as sprayed state. The results of stress-strain and fracture toughness were published in [21], the fatigue crack growth rate was published in a paper [24] together with the description of the complete testing methodology. On the basis of these two studies, it follows that near threshold behavior of cold sprayed pure metals is very similar to that of their bulk rolled counterparts. By increasing the cyclic load amplitude, however, the decohesion of individual spray particles takes place that lowers the fatigue crack growth resistance and fracture toughness K_{IC}.

316L steel

A similar combination of failure mechanisms was observed for the CS 316L steel and published in [22]. The transparticlular fracture was observed in the near threshold fatigue region, while the interparticular fracture was dominant at higher loads (see Fig. 3.16). In the same study we have shown that the interface quality can be improved significantly by heat treatment, by increasing the amount of transparticular fracture at higher loads.

Ti-6Al-4V

In addition to CS 316L steel, several groups of other industrially relevant materials were tested. Large experimental program was focused on Ti-6Al-4V alloy prepared by cold spray. It was one of the first attempts to describe the fracture anisotropy of the CS deposits. The transversal anisotropy of the material, corresponding to rotational symmetry of the splats, was

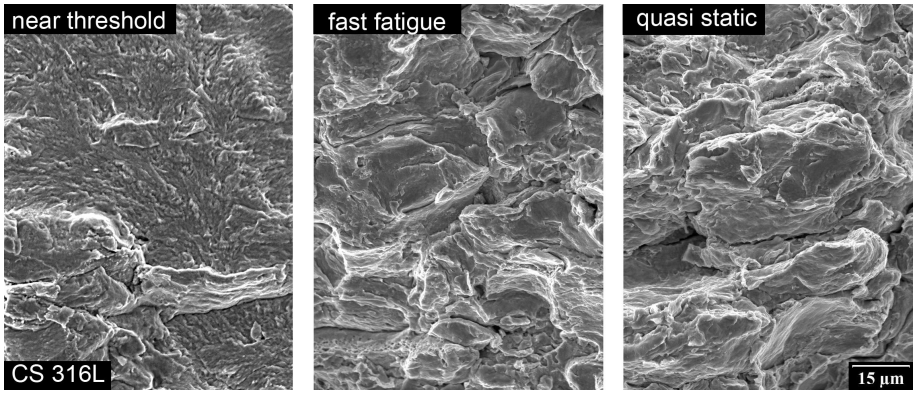

Figure 3.16: Transparticular morphology of fatigue fracture surface created by near threshold fatigue loading and interparticular fracture created at by at faster fatigue crack growth rate and at quasi-static loading during K_{IC} measurement.

described in the proceedings paper [27]. In the following testing of out of plane specimens, lower mechanical and fracture properties were obtained. The Decohesion dominated fracture mechanism was described, indicating low strength of interparticle interfaces. This study was complemented by an extensive investigation of in plane and out of plane samples deposited with the same spray conditions but subject to heat treatment. The obtained data are waiting to be published.

Metal matrix composites

Another materials under focus were diamond based MMCs (Al and Cu Matrix), which are abrasion resistant materials with excellent thermal conductivity. The results were published in a paper [25] that later received a "Best Paper Award" of Journal of Thermal Spray Technology [40]. The paper tries to explain the mechanical and fracture properties using the peening effect of stiff diamond particles that increases the matrix properties. Indirect evidence from instrumented indentation and X-ray supported this hypothesis.

Bell metal

A very traditional alloy, also called alloy A, was also investigated using the small specimen methodology. With a long term goal of cold spray repair of church bells, the bell metal, i.e. a Cu-20Sn tin bronze was cold sprayed on cast bell metal substrates. The measured mechanical and fracture properties were complemented with the results of the impact tests and compared to the cast material [26]. Encouraged by the good properties of the deposit, a small bell of approx 2.5 kg weight was cold sprayed to demonstrate good sound properties of the material, see Fig. 3.17. The research continues to improve the adhesion of the repair to the original substrate.

Figure 3.17: A small 2.5 kg bell additively manufactured by cold spray.

Al, the effect of powder size

The pure cold sprayed aluminum was investigated in a systematic study [36] trying to relate the input powder particle size, the $\eta = \frac{v_{\text{part}}}{v_{\text{crit}}}$ deposition parameter (see [99]) and the resulting mechanical and fracture properties. Here, v_{part} represents the particle velocity and v_{crit} represents the critical velocity at which the deposition efficiency is 50% %. The obtained results were complemented with the CS Al tested in previous studies [21] and [24]. For the observed CS Al deposits, the fatigue crack growth threshold ΔK_{thr} was linearly related to the yield strength YS_t (see Figure 3.18). In turn, the yield strength and corresponding deposit microstructure are shaped by work hardening and possible recrystallization at particle impact. On the other hand, no systematic relation of fracture toughness K_{IC} to yield strength was found.

Thermomechanically processed 6061 aluminum alloy

The paper [38] describes the effect of thermomechanical processing, namely the combination of hot rolling at reduction ratios of 10 to 40% (denoted as HRXX where XX is the rolling reduction in %) with subsequent solution annealing and aging (denoted SA) on stress-strain properties, fatigue strength, fatigue crack growth rate and fracture toughness. It was shown that hot rolling significantly increases ductility up to 4.2 % and strength up to 150 MPa. This increase was attributed to improved interparticular bonding. The subsequent aging treatment resulted in strength comparable to wrought and heat treated material, but with significantly decreased ductility. The highest ductility of the heat treated material was observed for the material rolled to a reduction

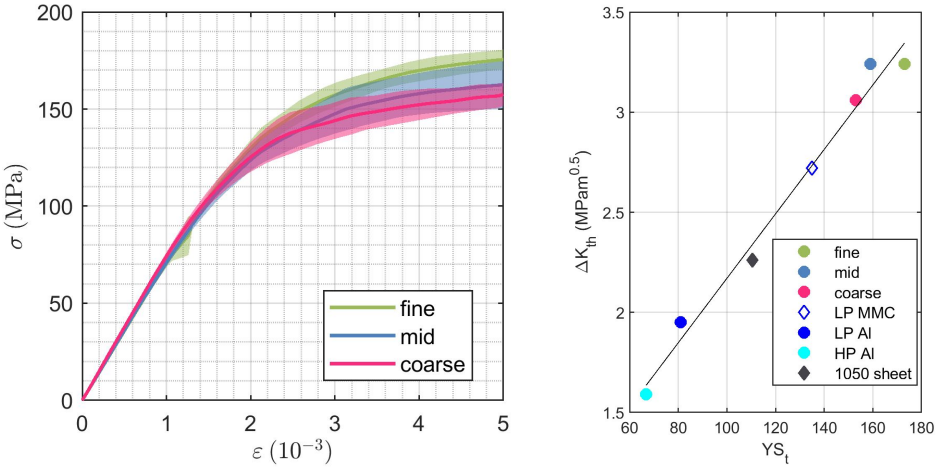

Figure 3.18: left: stress-strain curves of CS deposits from three Al powders investigated in [36]. right: relation of fatigue crack growth threshold ΔK_{thr} on yield stregth YS_t.

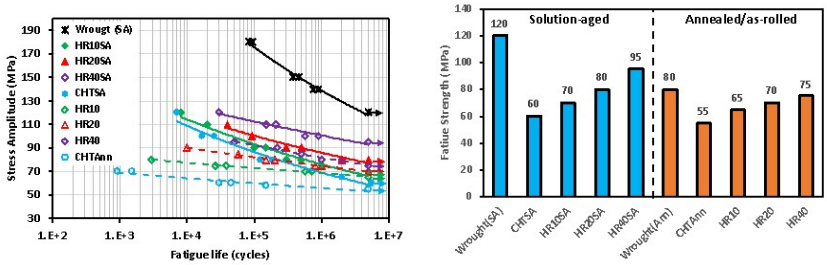

Figure 3.19: Fatigue strength and limit of CS 6061 aluminum alloy subjected to hot rolling (HR) and subsequent solution/aging heat treatment (SA).

of 40% reduction and reached around 2%. At the same time, rolling increased fracture properties, but subsequent heat treatment brought it back towards as-deposited material. In contrast, the fatigue strength was increased by both hot rolling and solution annealing. A hypothesis was formulated that fatigue cracks initiate on defects over the whole specimen cross-section (uniaxial loading was used) and accelerate the early stages of crack propagation by crack coalescence. The results of the fatigue and fracture property measurements are in Figs. 3.19 and 3.20. Once again, the acceleration of crack propagation by particle decohesion was observed fractographically for higher crack growth rates. Significant anisotropy was observed for the 40 % rolling reduction, as well as for materials after solution and aging treatment.

3.4.3 Modelling of fatigue crack growth rate

The data generated by the small specimen test methodology on both cold sprayed materials and their reference wrought counterparts were used in several studies to model the behavior $\frac{\mathrm{d}a}{\mathrm{d}N}(\Delta K)$ [28–31]. The fatigue crack

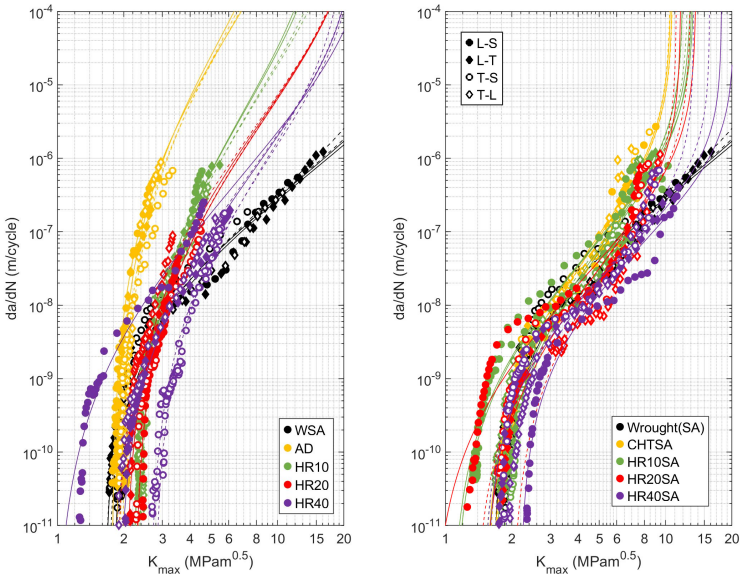

Figure 3.20: Fatigue crack growth rate curves of CS 6061 aluminum alloy subjected to hot rolling (HR) and subsequent solution/aging heat treatment (SA).

growth data, together with fracture toughness, allowed us to describe the effect of the crack driving force in the entire range from the threshold value ΔK_{thr} to dynamic fracture toughness A. Based on these studies, new Hartmann-Schijve formula fitting methods were developed as described in the chapter 3.1.7. This method was presented in [33] and fitted fatigue crack growth data for W base deposits is provided in Figure 3.15. The same methods was also used to fit data in recent papers such as [38], see Figure 3.20 or [37].

3.4.4 Directed energy deposition

Directed energy deposition represents an additive manufacturing technique in which the material is deposited into a small molten pool created by means of a laser or electron beam; see [100]. Complex review of laser based DMD methods is given e.g. in [101]. The method creates dense material with limited porosity; however, the extreme temperature gradients caused by the process may cause cracking. The resulting material often shows significant anisotropy as a result of the preferable heat flow direction during melt pool solidification. The fiber/cube texture of DMD In718 is compared with the pure transversally isotropic CS Al in Fig. 3.21 by electron backscatter diffraction (EBSD). The strong anisotropy of DMD material is a primary cause of the low elastic properties reported in many papers for this material with cubic crystal lattice, see, e.g. [102]. For cubic materials, the elastic, mechanical and fracture properties are similar when observed from several perpendicular directions as presented, e.g. in [35] for In738. Our subsequent testing of

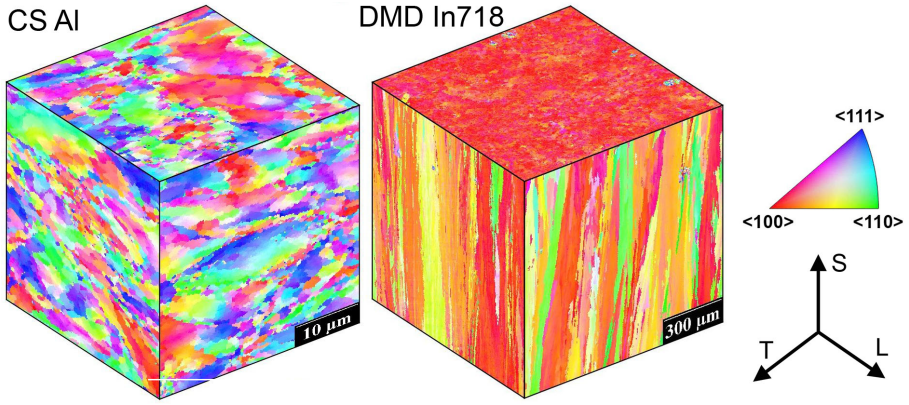

Figure 3.21: Pseudo 3D microstructure composed of EBSD IPF maps. Cold sprayed Al with transversal anisotropy and DMD Inconel 718 with fibrous anisotropy. Note the difference in scale.

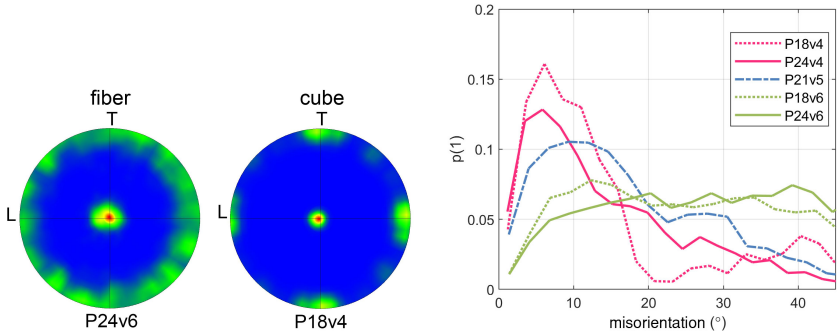

Figure 3.22: Grain boundary misorientation plot of DMD deposits with laser power P and scanning velocity v (e.g. P24v6 denotes $P = 2400$W and $v = 60$m/min). Pole figures of P24v6 indicates fiber textures, P14v4 illustrates cube texture.

the same material revealed that indeed much higher elastic modulus can be obtained for "diagonal" crystallographic directions such as [110], and even higher modulus can be expected for [111]. However, the investigation of fracture properties is quite complicated as these orientations have a higher crack growth resistance and the cracks are deflected out of their base plane, invalidating the testing results.

Further testing of DMD material was performed in a design of experiment study [37] that assessed the influence of process parameters, namely laser power and scanning speed on mechanical and fracture toughness of Inconel 718. It was found, that increasing the scanning speed above 50 m/min breaks the cube texture of the material and leads to high angle boundaries (see Fig. 3.22) causing solidification cracking. However, the size of the billets allowed the specimen to be loaded in a long scanning orientation only, and the observed effect of the process conditions on the mechanical and fracture properties was very weak.

Chapter 4

Conclusions and Outlook

The two previous chapters present different families of experimental methods. The flat specimen based methodology was aimed at investigating the fatigue life of surface treated specimens. The small specimen based methods were aimed at measuring the mechanical and fracture properties of materials available in small amounts, as well as investigating the anisotropy of these properties. Both families of experimental methods enabled us to enhance our knowledge of fatigue behavior and failure processes of conventional materials, coatings, and new additively manufactured materials.

The highlights of the large flat specimen testing can be summarized:

- Pioneering data on fatigue resistance and the failure mechanisms of thermally sprayed coatings were obtained [1].
- Fatigue crack growth has been observed directly in coated specimens [9].

The highlights of small specimen testing research are as follows:

- The robust method for fitting the vibration waveform allowed for the resonance excitation of the specimen and the simultaneous measurement of the fatigue crack growth rate [18]. This method provided a basis for a whole new class of fatigue crack growth and fatigue strength testing methods.
- Rate control - a direct control of crack propagation with a PID loop was established [19]. It solves the problem of non propagating cracks and enables the evaluation of the fatigue crack growth test time before the test.
- The method of inverse fit of the Hartmann-Schijve equation was developed [33] and implemented in a publicly available script.

The significance of the obtained results was indicated by several awards:

- The conference paper on the fatigue life of flat alumina coated specimens presented at the International Thermal Spray Conference 2004 (Orlando, Fl, USA) represented pioneering work in the study of fatigue failure processes in thermally sprayed materials. It was awarded a Certificate of

Merit and later published as an invited paper in the Journal of Thermal Spray Technology [1].

- The paper on fatigue crack propagation in Hastelloy X coated with yttria stabilized zirconia thermal barrier coating [9] was awarded Editors Choice of the Journal of Thermal Spray Technology in 2016.
- The paper on the mechanical and fracture properties of diamond-reinforced CS composites [25] received the Best Paper Award from the Journal of thermal Spray Technology for the year 2023 [40].
- Certificate of Merit was received at the International Thermal Spray Conference 2024 (Milan, IT) for the paper on the effect of the size of the feedstock particle on the mechanical and fracture properties of pure cold sprayed aluminum [36].

The investigation of mechanical and fracture properties, as well as failure processes, continues in the area of additively manufactured materials, where significant expertise has already been achieved. Recently, it was found that the small specimen testing method is well suited for the measurement of propagation rates of relatively short cracks. Thus, the methodology may significantly help in the effort to interconnect the fatigue limit of materials with their fracture mechanical properties. For example, the method is well suited to obtain the cyclic R-curves described in [103], which characterize the transition from physically short cracks to long cracks and may provide a suitable description of the crack initiation phase in AM materials containing defects. The first experiments were already performed on 12ChM steel and CSAM 6161 aluminum alloy (see Fig. 4.1) with promising results.

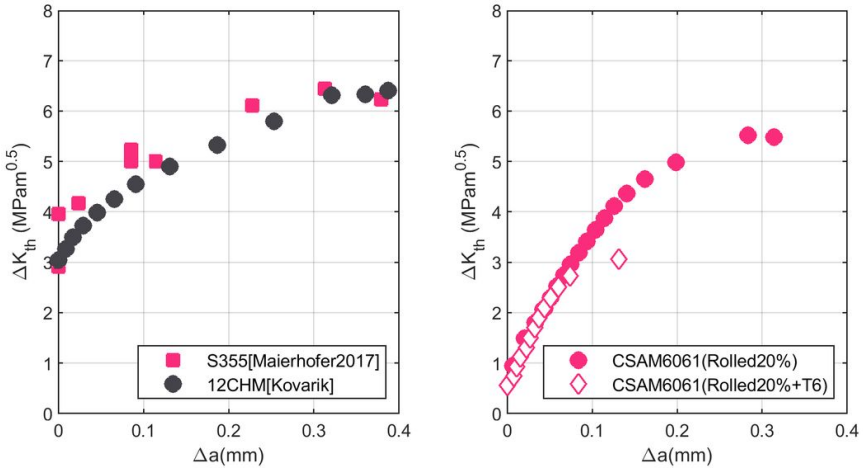

Figure 4.1: Cyclic R-curves for 12Chm steel (reference S355 data from [103]) and CSAM 6161 aluminum alloy.

It is the author's earnest wish that the methods described in this work will bring further exciting discoveries in the realm of fatigue and fracture mechanics of engineering materials.

Chapter 5

References

5.1 Flat specimen references

[1] O. Kovářík, J. Siegl, J. Nohava, and P. Chráska, Young's modulus and fatigue behavior of plasma-sprayed alumina coatings, *Journal of Thermal Spray Technology*, 14(2):231–238, 2005, doi:10.1361/105996304523809,

[2] O. Kovářík, J. Siegl, and Z. Procházka, Fatigue behavior of bodies with thermally sprayed metallic and ceramic deposits, *Journal of Thermal Spray Technology*, 17(4):525–532, 2008, doi:10.1007/s11666-008-9205-1,

[3] R. Mušálek, O. Kovářík, and J. Matějíček, In-situ observation of crack propagation in thermally sprayed coatings, *Surface and Coatings Technology*, 205(7):1807–1811, 2010, doi:10.1016/j.surfcoat.2010.03.064,

[4] J. Čížek, O. Kovářík, J. Siegl, K. A. Khor, and I. Dlouhý, Influence of plasma and cold spray deposited Ti layers on high-cycle fatigue properties of Ti6Al4V substrates, *Surface and Coatings Technology*, 217:23–33, 2013, doi:10.1016/j.surfcoat.2012.11.067,

[5] O. Kovářík, P. Haušild, J. Siegl, Z. Pala, J. Matějíček, and V. Davydov, The influence of plasma sprayed multilayers of Cr_2O_3 and Ni10wt%Al on fatigue resistance, *Surface and Coatings Technology*, 251:143–150, 2014, doi:10.1016/j.surfcoat.2014.04.018,

[6] R. Mušálek, O. Kovářík, J. Medřický, N. Curry, S. Bjorklund, and P. Nylen, Fatigue testing of TBC on structural steel by cyclic bending, *Journal of Thermal Spray Technology*, 24(1-2):168–174, 2014, doi:10.1007/s11666-014-0180-4,

[7] J. Čížek, M. Matějková, I. Dlouhý, F. Šiška, C. M. Kay, J. Karthikeyan, S. Kuroda, O. Kovářík, J. Siegl, K. Loke, and K. A. Khor, Influence of cold-sprayed, warm-sprayed, and plasma-sprayed layers deposition on fatigue properties of steel specimens, *Journal of Thermal Spray Technology*, 24(5):758–768, 2015, doi:10.1007/s11666-015-0240-4,

[8] O. Kovářík, P. Haušild, J. Čapek, J. Medřický, J. Siegl, R. Mušálek, Z. Pala, N. Curry, and S. Björklund, Resonance bending fatigue testing with simultaneous damping measurement and its application on layered coatings, *International Journal of Fatigue*, 82:300–309, 2016, doi:10.1016/j.ijfatigue.2015.07.026,

[9] O. Kovářík, P. Haušild, J. Medřický, L. Tomek, J. Siegl, R. Mušálek, N. Curry, and S. Björklund, Fatigue crack growth in bodies with thermally sprayed coating, *Journal of Thermal Spray Technology*, 25(1-2):311–320, jan 2016, doi:10.1007/s11666-015-0329-9,

[10] R. Mušálek, O. Kovářík, L. Tomek, J. Medřický, Z. Pala, P. Haušild, J. Capek, K. Kolarik, N. Curry, and S. Bjorklund, Fatigue performance of TBCs on Hastelloy X substrate during cyclic bending, *Journal of Thermal Spray Technology*, 25(1-2):231–243, 2016, doi:10.1007/s11666-015-0321-4,

[11] J. Čížek, O. Kovářík, F. Šiška, J. Bensch, J. Čupera, M. Matějková, J. Siegl, T. Chráska, and K. A. Khor, Increasing fatigue endurance of hydroxyapatite and rutile plasma sprayed biocomponents by controlling deposition in-flight properties, *ACS Biomaterials Science and Engineering*, 5(4):1703–1714, 2019, doi:10.1021/acsbiomaterials.8b01545,

[12] O. Kovářík, P. Haušild, J. Siegl, T. Chráska, J. Matějíček, Z. Pala, and M. Boulos, The influence of substrate temperature on properties of APS and VPS W coatings, *Surface and Coatings Technology*, 268:7–14, 2015, doi:10.1016/j.surfcoat.2014.07.041,

[13] O. Kovářík and J. Siegl, Microstructure and fracture morphology of thermally sprayed refractory metals and ceramics, *Strength of Materials*, 40(1):79–82, 2008, doi:10.1007/s11223-008-0021-0.

[14] O. Kovářík, P. Haušild, Z. Pala, P. Sachr, and V. Davydov, Effect of grit-blasting on residual stress field, *Key Engineering Materials*, 606:91–94, 2014, doi:10.4028/www.scientific.net/KEM.606.91.

[15] I. Tomáš, O. Kovářík, G. Vértesy, and J. Kadlecová, Nondestructive indication of fatigue damage and residual lifetime in ferromagnetic construction materials, *Measurement Science and Technology*, 25(6), 2014, doi:10.1088/0957-0233/25/6/065601,

[16] I. Tomáš, O. Kovářík, J. Kadlecová, and G. Vértesy, Optimization of fatigue damage indication in ferromagnetic low carbon steel, *Measurement Science and Technology*, 26(9), 2015, doi:10.1088/0957-0233/26/9/095603,

[17] R. Mušálek, J. Matějíček, M. Vilémová, and O. Kovářík, Non-linear mechanical behavior of plasma sprayed alumina under mechanical and thermal loading, *Journal of Thermal Spray Technology*, 19(1-2):422–428, 2010, doi:10.1007/s11666-009-9362-x,

5.2 Small specimen references

[18] O. Kovářík, A. Janča, and J. Siegl, Fatigue crack growth rate in miniature specimens using resonance, *International Journal of Fatigue*, 102:252–260, 2017, doi:10.1016/j.ijfatigue.2017.02.015,

[19] O. Kovářík, A. Materna, J. Siegl, J. Čížek, and J. Klecka, Fatigue crack growth in plasma-sprayed refractory materials, *Journal of Thermal Spray Technology*, 28(1-2):87–97, 2019, doi:10.1007/s11666-018-0790-3,

[20] O. Kovářík, J. Čech, J. Čapek, M. Hajíček, J. Klečka, and J. Siegl, Mechanical properties of forged tungsten heavy alloys, volume 27, pages 149–154, 2020, doi:10.14311/APP.2020.27.0149,

[21] O. Kovářík, J. Siegl, J. Čížek, T. Chráska, and J. Kondáš, Fracture toughness of cold sprayed pure metals, *Journal of Thermal Spray Technology*, 29(1-2):147–157, 2020, doi:10.1007/s11666-019-00956-z,

[22] S. Bagherifard, J. Kondáš, S. Monti, J. Čížek, F. Perego, O. Kovářík, F. Lukac, F. Gaertner, and M. Guagliano, Tailoring cold spray additive manufacturing of steel 316 l for static and cyclic load-bearing applications, *Materials and Design*, 203, 2021, doi:10.1016/j.matdes.2021.109575,

[23] O. Kovářík, J. Čížek, J. Klečka, M. Karlík, J. Čapek, J. Siegl, T. Chráska, and S. Takayasu, Mechanical properties and fatigue crack growth in tungsten deposited by RF-plasma, *Surface and Coatings Technology*, 410, 2021, doi:10.1016/j.surfcoat.2021.126930,

[24] J. Čížek, O. Kovářík, J. Čupera, J. Kondáš, T. Bajer, F. Šiška, M. Janovská, and H. Seiner, Measurement of mechanical and fatigue properties using unified, simple-geometry specimens: cold spray additively manufactured pure metals, *Surface and Coatings Technology*, 412, 2021, doi:10.1016/j.surfcoat.2021.126929,

[25] O. Kovářík, J. Čížek, S. Yin, R. Lupoi, M. Janovská, J. Čech, J. Čapek, J. Siegl, and T. Chráska, Mechanical and fatigue properties of diamond-reinforced cu and al metal matrix composites prepared by cold spray, *Journal of Thermal Spray Technology*, 31(1-2):217–233, 2022, doi:10.1007/s11666-022-01321-3,

[26] O. Kovářík, J. Daniel, J. Čížek, J. Kondáš, J. Čech, J. Siegl, and R. Singh, Fatigue properties of cold sprayed bell metal, In *International Thermal Spray Conference*. DVS Media GmbH, may 2022, doi:10.31399/asm.cp.itsc2022p0622,

[27] O. Kovářík, J. Čížek, and J. Kondáš, Anisotropy of Ti6Al4V deposited by cold spray, In *International Thermal Spray Conference*. DVS Media GmbH, may 2022, doi:10.31399/asm.cp.itsc2022p0756,

[28] R. Jones, O. Kovářík, S. Bagherifard, J. Čížek, and J. Lang, Damage tolerance assessment of am 304l and cold spray fabricated 316l steels and its implications for attritable aircraft, *Engineering Fracture Mechanics*, 254, 2021, doi:10.1016/j.engfracmech.2021.107916,

[29] R. Jones, J. Čížek, O. Kovářík, J. Lang, A. Ang, and J. G. Michopoulos, Characterising crack growth in Scalmalloy, volume 34, pages 39–44, 2021, doi:10.1016/j.prostr.2021.12.006,

[30] R. Jones, J. Čížek, O. Kovářík, A. Ang, and V. Champagne, Observations on comparable aluminium alloy crack growth curves: Additively manufactured Scalmalloy® as an alternative to AA5754 and AA6061-T6 alloys?, *Additive Manufacturing Letters*, 2:100026, apr 2022, doi:10.1016/j.addlet.2022.100026,

[31] R. Jones, O. Kovářík, J. Čížek, A. Ang, and J. Lang, Crack growth in conventionally manufactured pure nickel, titanium and aluminum and the cold spray additively manufactured equivalents, *Additive Manufacturing Letters*, 3:100043, dec 2022, doi:10.1016/j.addlet.2022.100043,

[32] A. Małachowska, O. Kovářík, A. Sajbura, P. Sokolowski, T. Lindner, M. Scholze, M. Karlík, J. Čech, and T. Lampke, Mechanical and fatigue properties of plasma sprayed (Fe0.9Co0.1)76Mo4(P0.45C0.2B0.2Si0.15)20 and Fe56.04Co13.45Nb5.5B25 metallic glasses, *Surface and Coatings Technology*, 459:129361, apr 2023, doi:10.1016/j.surfcoat.2023.129361,

[33] O. Kovářík, J. Čížek, and J. Klečka, Fatigue crack growth rate description of RF-plasma-sprayed refractory metals and alloys, *Materials*, 16(4):1713, feb 2023, doi:10.3390/ma16041713,

[34] O. Kovářík, J. Čížek, J. Klečka, M. Karlík, J. Čech, J. Kozlík, and H. Lauschmann, Tungsten Heavy Alloys from Mixed Feedstock by RF Plasma, *Journal of Thermal Spray Technology*, 32(8):2747–2762, Aug. 2023, doi:10.1007/s11666-023-01647-6,

[35] O. Kovářík, J. Čech, E. Kiziklioglu, J. Čížek, and T. Stittgen, Anisotropy of Mechanical Properties of DMD Build Inconel 738, In *Thermal Spray 2023: Proceedings from the International Thermal Spray Conference*, volume 84536 of *ITSC2023*, pages 473–479. ASM International, May 2023, doi:10.31399/asm.cp.itsc2023p0473,

[36] O. Kovářík, F. Wick, L. Wiehler, C. Huang, J. Čížek, A. List, F. Gärtner, and T. Klassen, The Effect of Powder Particle Size on Mechanical and Fracture Properties of Cold Sprayed Al, In *Thermal Spray 2024: Proceedings from the International Thermal Spray Conference*, volume 84864 of *ITSC2024*, pages 514–519. ASM International, Apr. 2024, doi:10.31399/asm.cp.itsc2024p0514,

[37] O. Kovářík, S. Maffia, T. Stittgen, F. Wick, V. Lukeš, and J. Čížek, Mechanical and Fracture Properties for As-Built 3DMD Inconel 718: Stability to Process Parameters Variation, In *Thermal Spray 2025: Proceedings from the International Thermal Spray Conference*, volume 85045 of *ITSC2025*, pages 434–441. ASM International, May 2025, doi:10.31399/asm.cp.itsc2025p0434,

[38] A. Nourian, O. Kovářík, J. Čížek, J. Čech, S. Zhue, T. Ando, and S. Müftü, Effect of thermo-mechanical treatment on the static and cyclic performance of cold sprayed 6061 aluminum alloy, *International Journal of Fatigue*, 201:109197, Dec. 2025, doi:10.1016/j.ijfatigue.2025.109197,

[39] O. Kovářík, Differential compliance from time domain vibration waveform fit and its application to fatigue crack growth rate testing, *International Journal of Fracture*, 249(4), Sept. 2025, doi:10.1007/s10704-025-00881-z,

[40] Journal of thermal spray technology volume 31 best paper awards, *Journal of Thermal Spray Technology*, 32(6):1573–1575, aug 2023, doi:10.1007/s11666-023-01628-9,

5.3 Other references

[41] *ASTM E647-15e1, Standard Test Method for Measurement of Fatigue Crack Growth Rates*, ASTM International, West Conshohocken, PA, 2015, doi:10.1520/E0647-15E01.

[42] G. Agricola, *Georgii Agricolae De re metallica : libri XII. Quibus officia, instrumenta, machinae, ac omnia deni[que] ad metallicam spectantia, non modo luculentissimè describuntur, sed & per effigies, suis locis infertas, adiunctis latinis, german*, Basileae :Apud Hieron. Frobenium et Nicolaum Episcopium,mense Martio., Basel, 1556, doi:10.5962/bhl.title.63737.

[43] R. E. Whan and A. I. H. Committee, *Materials characterization*, Number sv. 9,č. 10 in ASM handbook. American Society for Metals, 1986, URL `https://books.google.cz/books?id=cDu4XmtsRAIC`.

[44] H. Kuhn, D. Medlin, and A. I. H. Committee, *Mechanical testing and evaluation*, ASM handbook. ASM International, 2000, URL `https://books.google.cz/books?id=fdU6AQAAIAAJ`.

[45] S. Sampath, X. Jiang, A. Kulkarni, J. Matejicek, D. L. Gilmore, and R. A. Neiser, Development of process maps for plasma spray: Case study for molybdenum, *Materials Science and Engineering A*, 348(1-2):54–66, May 2003, doi:10.1016/S0921-5093(02)00642-1.

[46] M. Friis and C. Persson, Control of thermal spray processes by means of process maps and process windows, *Journal of Thermal Spray Technology*, 12(1):44–52, Mar. 2003, doi:10.1361/105996303770348492.

[47] P. Hosemann, Small-scale mechanical testing on nuclear materials: bridging the experimental length-scale gap, *Scripta Materialia*, 143:161–168, Jan. 2018, doi:10.1016/j.scriptamat.2017.04.026.

[48] M. S. Abdelrahman, W. Khalifa, and M. T. Abdu, Failure Analysis of Fatigue Failed M20 Class 8.8 Galvanized Steel Bolt, *Engineering Failure Analysis*, 150:107304, Aug. 2023, doi:10.1016/j.engfailanal.2023.107304.

[49] P. Haušild, A. Materna, and J. Nohava, On the identification of stress–strain relation by instrumented indentation with spherical indenter, *Materials amp; Design*, 37:373–378, May 2012, doi:10.1016/j.matdes.2012.01.025.

[50] M. Manahan, A. Argon, and O. Harling, The development of a miniaturized disk bend test for the determination of postirradiation mechanical properties, *Journal of Nuclear Materials*, 104:1545–1550, Jan. 1981, doi:10.1016/0022-3115(82)90820-0.

[51] G. Lucas, The development of small specimen mechanical test techniques, *Journal of Nuclear Materials*, 117:327–339, July 1983, doi:10.1016/0022-3115(83)90041-7.

[52] S. Taylor, S. Dhara, R. Beaumont, S. Krauss, A. Zeybek, and G. West, These ones are small; those ones are far away: A comparison of macro and in-situ micro tensile testing techniques, *Materialia*, 43:102533, Sept. 2025, doi:10.1016/j.mtla.2025.102533.

[53] M. Rund, R. Procházka, P. Konopík, J. Džugan, and H. Folgar, Investigation of Sample-size Influence on Tensile Test Results at Different Strain Rates, *Procedia Engineering*, 114:410–415, 2015, doi:10.1016/j.proeng.2015.08.086.

[54] T. Lube, M. Manner, and R. Danzer, The miniaturisation of the 4-point-bend test, *Fatigue amp; Fracture of Engineering Materials amp; Structures*, 20(11):1605–1616, Nov. 1997, doi:10.1111/j.1460-2695.1997.tb01514.x.

[55] X. Wang, T. Zhu, J. Zhang, H. Ding, S. Xiao, L. Lu, B. Yang, G. Yang, and Y. Liu, A review of selected small specimen test techniques for identifying deformation and failure properties of metallic materials, *Journal of Materials Science*, 58(1):63–100, Nov. 2022, doi:10.1007/s10853-022-07973-4.

[56] R. Pippan, S. Wurster, and D. Kiener, Fracture mechanics of micro samples: Fundamental considerations, *Materials amp; Design*, 159:252–267, Dec. 2018, doi:10.1016/j.matdes.2018.09.004.

[57] G. R. Odette and G. E. Lucas, An integrated approach to evaluating the fracture toughness of irradiated nuclear reactor pressure vessels, *Journal of Nondestructive Evaluation*, 15(3–4):137–150, Dec. 1996, doi:10.1007/bf00732041.

[58] Standard Test Methods for Tension Testing of Metallic Materials, doi:10.1520/e0008_e0008m-25.

[59] J. Dzugan, E. Lucon, M. Koukolikova, Y. Li, S. Rzepa, M. Yasin, S. Shao, N. Shamsaei, M. Seifi, M. Lodeiro, F. Lefebvre, U. Mayer, J. Olbricht, M. Houska, V. Mentl, and Z. You, ASTM interlaboratory study on tensile testing of AM deposited and wrought steel using miniature specimens, *Theoretical and Applied Fracture Mechanics*, 131:104410, June 2024, doi:10.1016/j.tafmec.2024.104410.

[60] A. S. M. Ang and C. C. Berndt, A review of testing methods for thermal spray coatings, *International Materials Reviews*, 59(4):179–223, May 2014, doi:10.1179/1743280414Y.0000000029.

[61] C. M. Kay and J. Karthikeyan, *High pressure cold spray: principles and applications*, ASM International, 2016, URL `https://books.google.cz/books?id=uSvJjwEACAAJ`.

[62] C. K. Chua, C. H. Wong, and W. Y. Yeong, Material Characterization for Additive Manufacturing, In *Standards, quality control, and measurement sciences in 3D printing and additive manufacturing*, pages 95–137. Elsevier, Jan. 2017, doi:10.1016/b978-0-12-813489-4.00005-2.

[63] E. F. Rybicki, J. R. Shadley, Y. Xiong, and D. J. Greving, A cantilever beam method for evaluating Young's modulus and Poisson's ratio of thermal spray coatings, *Journal of Thermal Spray Technology*, 4(4):377–383, Dec. 1995, doi:10.1007/BF02648639.

[64] H. Herbert, Ueber den Zusammenhang der Biegungselastizität des Gußeisens mit seiner Zug- und Druckelastizität, *Forschungsarbeiten auf dem Gebiete des Ingenieurwesens*, pages 39–81, 1910, doi:10.1007/978-3-662-02218-4_2.

[65] *E1820-18ae12019, Standard test method for measurement of fracture toughness*, ASTM International, West Conshohocken, PA, 2019, doi:10.1520/E1820-18AE01.

[66] R. T. R. R. Mcgrann, D. J. Greving, J. R. Shadley, E. F. Rybicki, B. E. Bodger, and D. A. Somerville, The effect of residual stress in HVOF tungsten carbide coatings on the fatigue life in bending of thermal spray coated aluminum, *Journal of Thermal Spray Technology*, 7(4):546–552, Dec. 1998, doi:10.1361/105996398770350774.

[67] S. Watanabe, J. Amano, T. Tajiri, and N. Sakoda, Fatigue cracks in HVOF thermally sprayed WC-Co coatings, *Journal of Thermal Spray Technology*, 7(1):93–96, Mar. 1998, doi:10.1361/105996398770351098.

[68] A. Ibrahim, R. S. Lima, C. C. Berndt, B. M. S. Coatings, and undefined 2007, Fatigue and mechanical properties of nanostructured and conventional titania (TiO2) thermal spray coatings, *Surface and Coatings Technology*, 201(16–17):7589–7596, May 2007, doi:10.1016/j.surfcoat.2007.02.025.

[69] W. A. González-Hermosilla, D. Chicot, J. Lesage, J. G. La Barbera-Sosa, I. C. Gruescu, M. H. Staia, and E. S. Puchi-Cabrera, Effect of substrate roughness on the fatigue behavior of a SAE 1045 steel coated with a WC-10Co-4Cr cermet, deposited by HVOF thermal spray, *Materials Science and Engineering A*, 527(24-25):6551–6561, Sept. 2010, doi:10.1016/j.msea.2010.07.014.

[70] H. J. C. Voorwald, L. F. S. Vieira, and M. O. H. Cioffi, Evaluation of WC-10Ni thermal spraying coating by HVOF on the fatigue and corrosion AISI 4340 steel, In *Procedia Engineering*, volume 2, pages 331–340. Elsevier, Apr. 2010, doi:10.1016/j.proeng.2010.03.037.

[71] V. Higuera, F. J. Belzunce, J. R. S. Technology, Coatings, and undefined 2006, Influence of the thermal-spray procedure on the properties

of a CoNiCrAlY coating, *Elsevier*, 200(18–19):5550–5556, May 2006, doi:10.1016/j.surfcoat.2005.07.070.

[72] A. Ibrahim and C. C. Berndt, Fatigue and deformation of HVOF sprayed WC-Co coatings and hard chrome plating, *Materials Science and Engineering A*, 456(1-2):114–119, May 2007, doi:10.1016/j.msea.2006.12.030.

[73] R. McGrann, D. Greving, J. Shadley, E. Rybicki, T. Kruecke, and B. Bodger, The effect of coating residual stress on the fatigue life of thermal spray-coated steel and aluminum, *Surface and Coatings Technology*, 108–109:59–64, Oct. 1998, doi:10.1016/s0257-8972(98)00665-3.

[74] M. P. Nascimento, R. C. Souza, W. L. Pigatin, and H. J. C. Voorwald, Effects of surface treatments on the fatigue strength of AISI 4340 aeronautical steel, *International Journal of Fatigue*, 23(7):607–618, Aug. 2001, doi:10.1016/S0142-1123(01)00015-9.

[75] E. S. Puchi-Cabrera, M. H. Staia, Y. S. S. . . . , Coatings, and undefined 2013, Fatigue behavior of AA7075-T6 aluminum alloy coated with a WC–10Co–4Cr cermet by HVOF thermal spray, *Surface and Coatings Technology*, 220:122–130, Apr. 2013, doi:10.1016/j.surfcoat.2012.04.087.

[76] R. C. Souza, H. J. C. Voorwald, M. C. S. Technology, Coatings, and undefined 2008, Fatigue strength of HVOF sprayed Cr3C2–25NiCr and WC-10Ni on AISI 4340 steel, *Elsevier*, 203(3–4):191–198, Nov. 2008, doi:10.1016/j.surfcoat.2008.07.038.

[77] P. J. Patt, Frictionless motor material testing, 2002, URL `https://patents.google.com/patent/US6405599B1/en`.

[78] IEEE standard for digitizing waveform recorders, *IEEE Std 1057-1994*, 1994, doi:10.1109/IEEESTD.1994.122649.

[79] P. Haušild and J. Siegl, The influence of contaminated He exposure on fracture toughness of steels A316 and P91, Research report in Czech V-KMAT-767/09, FNSPE, CTU, 2009.

[80] A. Puškár, *Internal friction of materials*, Cambridge International Science Publishing, Cambridge, UK, 2003.

[81] V. P. Golub, V. P. Butseroga, and A. D. Pogrebnyak, Study of the kinetics of fatigue cracks by the method of differential compliance, *International Applied Mechanics*, 31(12):1018–1025, Dec. 1995, doi:10.1007/BF00847262.

[82] A. Saxena and S. J. Hudak, Review and extension of compliance information for common crack growth specimens, *International Journal of Fracture*, 14(5):453–468, 1978, doi:10.1007/BF01390468.

[83] J. C. Newman, Y. Yamada, and M. A. James, Back-face strain compliance relation for compact specimens for wide range in crack lengths, *Engineering Fracture Mechanics*, 78(15):2707–2711, Oct. 2011, doi:10.1016/j.engfracmech.2011.07.001.

[84] T. G. Chondros, A. D. Dimarogonas, and J. Yao, A continuous cracked beam vibration theory, *Journal of Sound and Vibration*, 215(1):17–34, Aug. 1998, doi:10.1006/jsvi.1998.1640.

[85] T. Fett, Stress intensity factors, T-stresses, weight functions, Technical report, 2008, doi:10.5445/KSP/1000007996.

[86] M. Tenenbaum and H. Pollard, *Ordinary differential equations : an elementary textbook for students of mathematics, engineering, and the sciences*, Dover Publications, 1985.

[87] G. A. F. Seber and C. J. Wild, *Nonlinear Regression*, Wiley Series in Probability and Statistics. John Wiley & Sons, Inc., Hoboken, NJ, USA, Feb. 1989, doi:10.1002/0471725315.

[88] P. R. Edwards and J. J. C. Newman, Short-crack growth behaviour in various aircraft materials, Technical Report AGARD-R-767, NASA Langley Research Center, 1990.

[89] J. C. Newman Jr, X. R. Wu, S. L. Venneri, and C. G. Li, Small-crack effects in high-strength aluminum alloys a NASA/CAE cooperative program, Technical Report NASA RP-1309, NASA Langley ResearchCenter, 1994.

[90] A. S. T. M. Internationa, ASTM Standard D 399-09: Standard test method for linear-elastic plane-strain fracture toughness K_{IC} of metallic materials, 2009, doi:10.1520/E0399-09E02.2.

[91] Z. He, A. Kotousov, and R. Branco, Evaluation of fatigue crack front shape for a specimen with finite thickness, In *MATEC Web of Conferences*, volume 28, page 01004. EDP Sciences, Oct. 2015, doi:10.1051/matecconf/20152801004.

[92] C. Benz and M. Sander, Fatigue crack growth testing at negative stress ratios: discussion on the comparability of testing results, *Fatigue &Fracture of Engineering Materials & Structures*, 37(1):62–71, July 2013, doi:10.1111/ffe.12082.

[93] X. Sun, G. Liu, X. Liang, and S. Tong, Superior comprehensive mechanical properties of a low-carbon medium manganese steel for replacing AISI 4330 steel in the oil and gas industry, *Materials*, 16(2):490, Jan. 2023, doi:10.3390/ma16020490.

[94] J. Newman, M. James, and W. Johnson, Fatigue crack growth threshold testing of metallic rotorcraft materials, Technical Report ARL-TR-4472, 2013.

[95] K.-H. Schwalbe, S. Kalluri, R. M. McGaw, A. Neimitz, and S. W. Dean, On the beauty of analytical models for fatigue crack propagation and fracture—a personal historical review, *Journal of ASTM International*, 7(8):102713, 2010, doi:10.1520/jai102713.

[96] T. F. Coleman and Y. Li, An interior trust region approach for nonlinear minimization subject to bounds, *SIAM Journal on Optimization*, 6(2):418–445, may 1996, doi:10.1137/0806023.

[97] G. V. Guinea, J. Y. Pastor, J. Planas, and M. Elices, Stress intensity factor, compliance and CMOD for a general three-point-bend beam, *International Journal of Fracture*, 89(2):103–116, 1998, doi:10.1023/a:1007498132504.

[98] R. A. Mayville and I. Finnie, Uniaxial stress-strain curves from a bending test, *Experimental Mechanics*, 22(6):197–201, June 1982, doi:10.1007/bf02326357.

[99] H. Assadi, T. Schmidt, H. Richter, J.-O. Kliemann, K. Binder, F. Gärtner, T. Klassen, and H. Kreye, On parameter selection in cold spraying, *Journal of Thermal Spray Technology*, 20(6):1161–1176, June 2011, doi:10.1007/s11666-011-9662-9.

[100] B. Dutta, S. Babu, and B. Jared, *Metal additive manufacturing*, volume Additive Manufacturing Materials and Technologies, Elsevier, 2019, doi:10.1016/b978-0-12-816634-5.00001-7.

[101] S. M. Thompson, L. Bian, N. Shamsaei, and A. Yadollahi, An overview of Direct Laser Deposition for additive manufacturing; Part I: Transport phenomena, modeling and diagnostics, *Additive Manufacturing*, 8:36–62, Oct. 2015, doi:10.1016/j.addma.2015.07.001.

[102] G. Dinda, A. Dasgupta, and J. Mazumder, Texture control during laser deposition of nickel-based superalloy, *Scripta Materialia*, 67(5):503–506, sep 2012, doi:10.1016/j.scriptamat.2012.06.014.

[103] J. Maierhofer, S. Kolitsch, R. Pippan, H.-P. Gänser, M. Madia, and U. Zerbst, The cyclic R-curve – Determination, problems, limitations and application, *Engineering Fracture Mechanics*, 198:45–64, July 2018, doi:10.1016/j.engfracmech.2017.09.032.